Article

Developmental Cell

Mechano-electrical transduction components TMC1-CIB2 undergo a Ca^{2+}-induced conformational change linked to hearing loss

Graphical abstract

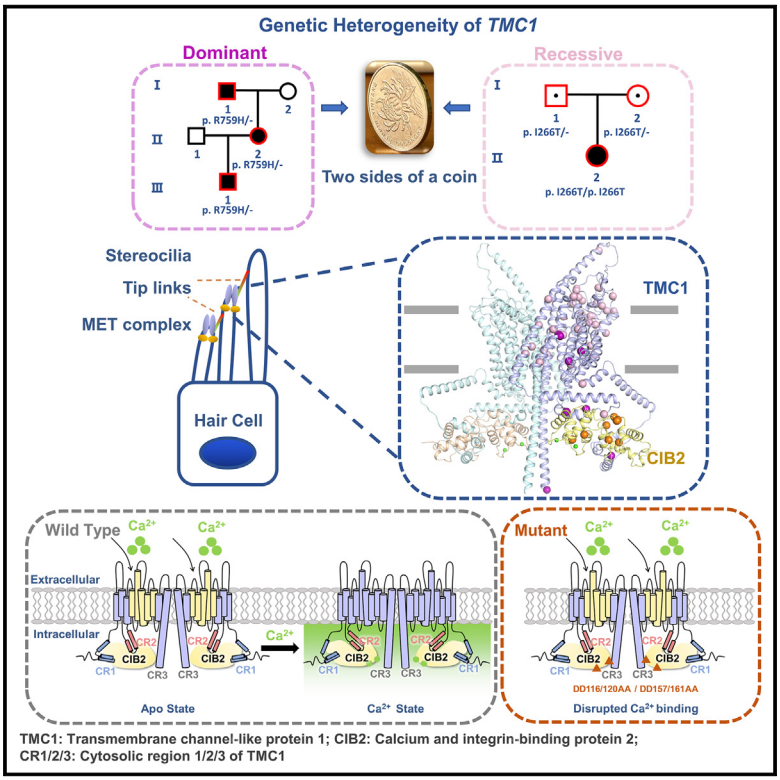

Highlights

- Ca^{2+} binding induces a conformational change in the TMC1-CIB2 complex
- A vertebrate-specific site on TMC1 can bind with *apo*-CIB2
- Disrupting CIB2 Ca^{2+} binding sites impairs MET function in *ex vivo* cochlea models
- Dominant TMC1 mutations cluster around the ion pore or the CIB2-binding interface

Authors

Shaoxuan Wu, Lin Lin, Qiaoyu Hu, ..., Zhigang Xu, Fang Bai, Qing Lu

Correspondence

wqcr301@vip.sina.com (Q.W.), xuzg@sdu.edu.cn (Z.X.), baifang@shanghaitech.edu.cn (F.B.), luqing67@sjtu.edu.cn (Q.L.)

In brief

Wu et al. identify a Ca^{2+}-regulated coupling between mammalian TMC1 and CIB2 by combining *in vitro*, *in silico*, and *ex vivo* methods. This study shows how structural changes perturb channel function and provide insight into the understanding of genetic heterogeneity of *TMC1* in hearing loss.

Wu et al., 2025, Developmental Cell *60*, 1586–1600
June 9, 2025
https://doi.org/10.1016/j.devcel.2025.01.004

CellPress

CellPress

Developmental Cell

Article

Mechano-electrical transduction components TMC1-CIB2 undergo a Ca^{2+}-induced conformational change linked to hearing loss

Shaoxuan Wu,[1,14] Lin Lin,[1,14] Qiaoyu Hu,[2,10,14] Xuebo Yao,[3,14] Hongyang Wang,[4,14] Shuang Liu,[5] Qingling Liu,[5] Yuehui Xi,[3] Yuzhe Lin,[6,11,12] Jianqiao Gong,[1] Ruixing Hu,[1] Wei Zhan,[7] Yi Luo,[4] Guang He,[1] Zhijun Liu,[7] Wei Xiong,[5] Qiuju Wang,[4,*] Zhigang Xu,[3,*] Fang Bai,[2,8,9,13,*] and Qing Lu[1,6,11,12,15,*]

[1]Bio-X Institutes, Key Laboratory for the Genetics of Developmental and Neuropsychiatric Disorders, Ministry of Education, Shanghai Jiao Tong University, Shanghai 200030, China
[2]Shanghai Institute for Advanced Immunochemical Studies, ShanghaiTech University, Shanghai 201210, China
[3]Shandong Provincial Key Laboratory of Animal Cells and Developmental Biology and Key Laboratory for Experimental Teratology of the Ministry of Education, School of Life Sciences, Shandong University, Qingdao, Shandong 266237, China
[4]Senior Department of Otolaryngology, Head and Neck Surgery, Department of Audiology and Vestibular Medicine, Chinese PLA Institute of Otolaryngology, Chinese PLA General Hospital, Medical School of Chinese PLA, Beijing 100853, China
[5]Chinese Institute for Brain Research, Beijing 102206, China
[6]Department of Otolaryngology-Head and Neck Surgery, Shanghai Ninth People's Hospital, Shanghai Jiao Tong University School of Medicine, Shanghai, China
[7]National Facility for Protein Science in Shanghai, Shanghai Advanced Research Institute, Chinese Academy of Science, Zhangjiang Lab, Shanghai 201210, China
[8]School of Information Science and Technology, ShanghaiTech University, Shanghai 201210, China
[9]Shanghai Clinical Research and Trial Center, Shanghai 201210, China
[10]Innovation Center for AI and Drug Discovery, School of Pharmacy, East China Normal University, Shanghai 200062, China
[11]Ear Institute, Shanghai Jiao Tong University School of Medicine, Shanghai, China
[12]Shanghai Key Laboratory of Translational Medicine on Ear and Nose Diseases, Shanghai, China
[13]School of Life Science and Technology, ShanghaiTech University, Shanghai 201210, China
[14]These authors contributed equally
[15]Lead contact
*Correspondence: wqcr301@vip.sina.com (Q.W.), xuzg@sdu.edu.cn (Z.X.), baifang@shanghaitech.edu.cn (F.B.), luqing67@sjtu.edu.cn (Q.L.)
https://doi.org/10.1016/j.devcel.2025.01.004

SUMMARY

TMC1, a unique causative gene associated with deafness, exhibits variants with autosomal dominant and recessive inheritance patterns. *TMC1* codes for the transmembrane channel-like protein 1 (TMC1), a key component of the mechano-electrical transduction (MET) machinery for hearing. However, the molecular mechanism of Ca^{2+} regulation in MET remains unclear. Calcium and integrin-binding protein 2 (CIB2), another MET component associated with deafness, can bind with Ca^{2+}. Our study shows that TMC1-CIB2 complex undergoes a Ca^{2+}-induced conformational change. We identified a vertebrate-specific binding site on TMC1 that interacts with *apo* CIB2, linked with hearing loss. Using an *ex vivo* mouse organotypic cochlea model, we demonstrated that disruption of the calcium-binding site of CIB2 perturbs the MET channel conductivity. After systematically analyzing the hearing loss variants, we observed dominant mutations of TMC1 cluster around the putative ion pore or at the binding interfaces with CIB2. These findings elucidate the molecular mechanisms underlying *TMC1*-linked hearing loss.

INTRODUCTION

Hearing loss affects an estimated 5% of the world's population, making it a prevalent sensory deficit in humans. Over 150 genes and 8,000 variants have been implicated in the pathogenesis of hearing loss,[1] highlighting the heterogeneity of this condition and the need for gene-specific or variant-specific phenotype studies. *TMC1* (OMIM*606706) is a commonly implicated gene in genetic hearing loss,[2–7] with two distinct phenotypes. Variants in *TMC1* have been associated with both autosomal dominant and autosomal recessive hearing loss,[8–11] located separately at DFNA36 and DFNB7/11, and present distinct clinical phenotypes. DFNB7/11 is characterized by congenital severe to profound hearing loss, with a minority of patients presenting with moderate hearing loss. On the other hand, DFNA36 is featured by acquired or postlingual progressive hearing loss.[9,11–13] Accurate genetic variant classification is crucial for proper genetic diagnoses, but this remains a major challenge in the post-genome era.

In the auditory system, the mechano-electrical transduction (MET) protein machinery in the cochlear hair cells is responsible for sound perception.[14–16] The MET machinery is located in the actin-based protrusions, known as stereocilia, which are organized in a staircase-like structure. Soundwaves trigger the deflection of stereocilia, causing the MET channels to open, leading to the influx of K^+ and Ca^{2+} ions and altering receptor potential.[17] Several proteins have been identified as the components of the mammalian hair cell MET machinery, including the transmembrane (TM)-like channel 1 and 2 (TMC1 and TMC2),[11,18–20] cadherin 23 (CDH23),[21] protocadherin-15 (PCDH15),[22,23] lipoma HMGIC fusion partner-like 5 (LHFPL5),[24,25] TM inner ear (TMIE),[26,27] and calcium and integrin-binding protein 2 and 3 (CIB2 and CIB3).[28–31] TMC1 and TMC2 are pore-forming subunits of the MET channel and can act as a mechanosensor.[19,20,32–35] CIB2 and CIB3, as cytosolic proteins, play a crucial role in MET complex assembly.[30,31,36,37] Variants of *TMC1* and *CIB2* genes have been linked to hearing loss.[8,11,29,38–41] Recent studies have determined the TMC1/2-CALM1-TMIE complex structure in worms.[42,43] However, the molecular mechanisms underlying mammalian MET assembly, maintenance, and gating kinetics for hearing remain to be fully elucidated.

The hair cell MET channel, in comparison with other mechanosensitive channels, exhibits remarkably fast open-close kinetics that enable it to respond to fluctuating sound input. The gating kinetics of the channel (activation, fast adaptation, and slow adaptation) are functionally modulated by biophysical and pharmacological factors including Ca^{2+}. The roles of Ca^{2+} in MET gating are incredibly intriguing, including extracellular (EC) Ca^{2+} homeostasis and intracellular Ca^{2+}-dependent adaptation.[44–48] However, it is important to note that the role of Ca^{2+} in the adaptation of mammalian cochlear hair cells remains debatable.[48–50] The concentration of Ca^{2+} in the scala media, at 20 μM, maintains the stereocilia's stiffness and rigidity.[44,45,51] An influx of Ca^{2+} modulates the activation and adaptation of the transducer current.[46–48] CIB2, a Ca^{2+}-binding protein and critical binding partner of TMC1, whose null mutation in mice result in abolished mechanotransduction currents, may play essential role of the intracellular Ca^{2+}-mediated modulation on the MET channel kinetics.

CIB2 consists of four EF-hands (helix-loop-helix, Ca^{2+}-binding motif).[52] Calmodulin and CaBP1, as well-studied members of the EF-hand-containing superfamily, are Ca^{2+} sensors for voltage-gated sodium channels and Ca^{2+} channels (CaV1.2 and CaV1.3, collectively called CaV).[53–55] After the opening of CaV channels, an increase of cytosolic Ca^{2+} levels lead to Ca^{2+}-bound calmodulin modulating the conductivity of CaV and facilitating rapid Ca^{2+}-dependent channel inactivation.[56] Our study demonstrates that the CIB2-TMC1 complex undergoes conformational changes in response to calcium, and the calcium-binding elements of CIB2 are essential for the proper function of the MET channel in sound perception. Additionally, we have characterized disease mutations that interfere with the TMC1-CIB2 interactions through structural analysis, biochemical validation, and *ex vivo* assays, thoroughly investigating the clinical phenotypes from micro to macro.

RESULTS

The complex structure of mammalian CIB2 and TMC1 CR1

Previous studies have shown that two cytosolic regions (CRs) of TMC1 (CR1, amino acids 81–130 and CR2, amino acids 303–347) (Figure 1A) bind to CIB2/CIB3 and have reported the complex structures of TMC1 CR2-CIB3.[29,30] The recently reported complex structure of the worm TMC1-CALM1 complex lacks the details about the interaction between TMC1 CR1 and CIB2 due to resolution limitations.[42] To gain a better understanding of the atomic level interaction between the mammalian TMC1 CR1 and CIB2, we co-crystallized the protein complex of mouse TMC1 CR1 and CIB2. We then successfully solved the mammalian complex structure at a resolution of 1.74 Å (Table S1).

In the complex structure, the overall fold of CIB2 is very similar to other CIB family proteins, but the binding mode between CIB2 and TMC1 CR1 is entirely unexpected. CIB2 has nine α helices (h1 to h9) forming four EF-hands, with only EF-hands 3 and 4 of CIB2 binding Ca^{2+} (Figure S1). TMC1 CR1 folds into three short α helices (H1–H3) (Figure 1B), binding with the N-terminal region of CIB2. In contrast, in the structure of TMC1 CR2 and CIB3 complex, CR2 folds into two α helices and contacts with a hydrophobic trench at the C-terminal of CIB3.[30]

The interface between TMC1 CR1 and CIB2 buries a surface area of about 740.9 $Å^2$ between these two molecules. TMC1 CR1 contacts the N-terminal region of CIB2, involving h1, h2, and h4–h6. TMC1 CR1-CIB2 interface is mainly mediated by electrostatic interactions, hydrogen bonds, and hydrophobic interactions. R85 and K101 of TMC1 form hydrogen bonds with Q17 and the main chain of T20 of CIB2, respectively (Figure 1C). C102 and P104 from the linker between H1 and H2 of TMC1 contact with the hydrophobic groove formed by F78, V97, L106, and Y110 (Figure 1D). In addition, K106, K110, and K118 of TMC1 form salt bridges with D90, D93, and D18 of CIB2, respectively (Figure 1D). Hydrophobic interactions exist among M107, I111 from CR1 and Y16, C19, and V92 from CIB2 (Figure 1E). The sequence alignment of TMC1 CR1 region among different species indicates that the residues involved in TMC1 interaction are highly conserved in vertebrates but less conserved in worm TMC1 (Figure 1F). Consistently, mutations (CIB2-DD90/93KK and CR1-KK106/110DD) that disrupt these polar interactions weakened or even abolished the TMC1 CR1-CIB2 interaction in isothermal titration calorimetry (ITC) assays (Figure 1G). Based on the structure superimposition of TMC1 CR1-CIB2 and TMC1 CR2-CIB3 (Figure 1H), we found that the two binding surfaces of CR1 and CR2 are located at opposite ends of CIB2/CIB3, suggesting the possibility of CR1 and CR2 binding to CIB2 simultaneously and the potential existence of additional undiscovered CIB2-binding sites. On the other hand, CIB2 belongs to the EF-hand family, which includes calmodulin, a well-characterized calcium sensors that participates in various physiological processes.[57–59] This led us to consider the calcium-binding property of CIB2's EF-hands.

Ca^{2+}-mediated regulation on the binding between CIB2 and TMC1 CRs

The high-resolution complex structure mentioned above prompted us to conduct an extensive biochemical characterization of

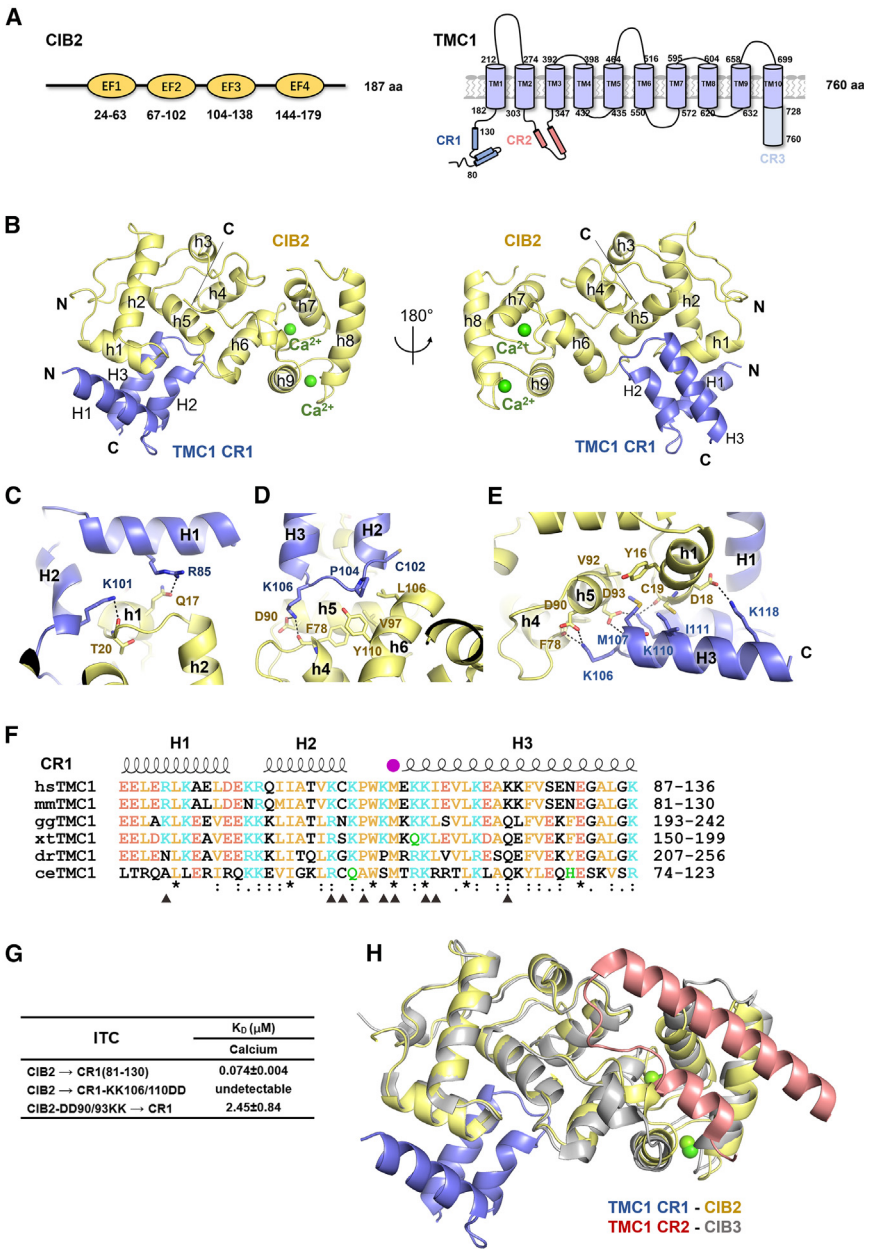

Figure 1. Crystal structure of the mammalian TMC1 CR1-CIB2 complex

(A) Schematic diagrams show the organization of the EF-hand domains of CIB2, transmembrane helices, and CRs of TMC1.

(B) Ribbon diagram representation of the TMC1 CR1-CIB2 structure as viewed from the front (left) and the back (right); secondary structure elements are labeled.

(C–E) Detailed interactions between CIB2 and TMC1 CR1. Residues involved in protein interaction are shown with the stick model. CIB2 and TMC1 CR1 are colored in slate and pale yellow, respectively. Hydrogen bonds are shown as black dashed lines.

(F) Sequence alignments of TMC1 CR1 from different species. The secondary structural elements of TMC1 CR1 determined from this work are shown above its alignment. Conserved residues are colored orange (nonpolar), green (polar), blue (positive charged), and red (negative charged). Specifically, residues indicated with black triangles are responsible for the interaction between CIB2 and TMC1 CR1; the dominant disease mutation site is indicated with a purple circle. hs, *Homo sapiens*; mm, *Mus musculus*; gg, *Gallus gallus*; xt, *Xenopus tropicalis*; dr, *Danio rerio*; ce, *Caenorhabditis elegans*.

(G) Summary of the binding affinities between WT or structural mutants of CIB2 and TMC1 CR1. See also Figure S7C.

(H) Model alignment of TMC1 CR1-CIB2 with TMC1 CR2-CIB3 (PDB: 6WUD). See also Table S1.

CIB2's binding to different TMC1 CRs and its interaction with calcium (Figures 1A, 2A, and 2B). Upon detailed examination of all CRs of TMC1, we discovered an additional binding site in TMC1 C-terminal, named TMC1 CR3 (amino acids 718–757, at the extreme C-terminal of TMC1 TM10). Sequence alignment showed that CR3 region is only conserved among vertebrates, emerging with the presence of the inner ear (Figure 2B). To quantitatively analyze the binding affinity, we performed ITC assays to measure the dissociation constant (K_D) under conditions with or without calcium. In the presence of calcium, CIB2 bound to CR1 and CR2 with the K_D values of ~0.074 and ~0.48 μM, respectively (Figure 2C). Without calcium, the binding affinity of CIB2-CR1 and CIB2-CR2 decreased to ~0.87 and ~ 10.8 μM. Unlike CR1 and CR2, CR3 can only form complexes with CIB2 in the absence of calcium, with a binding affinity of ~43.4 μM (Figure 2C).

To elucidate the formation of the complex, we utilized size-exclusion chromatography coupled with multi-angle static light scattering (SEC-MALS) to determine the molar mass of the complex. First, upon introducing Ca^{2+} to the CIB2-CR1 complex, we observed a shift to a higher elution volume, suggesting the presence of Ca^{2+} induced a conformational change in the CIB2-CR1 complex (Figure 2D). In the case of CIB2-CR2, we observed a molar mass increase and a ~200-fold increase in binding affinity (Figure 2C). These findings indicate a more significant conformational modulation on CIB2-CR2 mediated by Ca^{2+}. Regarding the CIB2-CR3 complex, we found that CIB2 forms a complex with CR3 only in the absence of calcium, which is consistent with the ITC data. To understand the composition of the mixture of CIB2 with CR1 and CR2 under calcium conditions, we determined the molar mass and discovered a binding ratio of 1:1:1 for CIB2:CR1:CR2 (Figures 2E and 2F). This supports the prediction made by our structure analysis that both CR1 and CR2 can simultaneously bind to CIB2. Similarly, in the *apo* state (absence of calcium), the mixture of CIB2 with CR1 and CR3 also displayed a binding ratio of 1:1:1 for CIB2:CR1:CR3, indicating the simultaneous binding of CR1 and CR3 (Figures 2E and 2F).

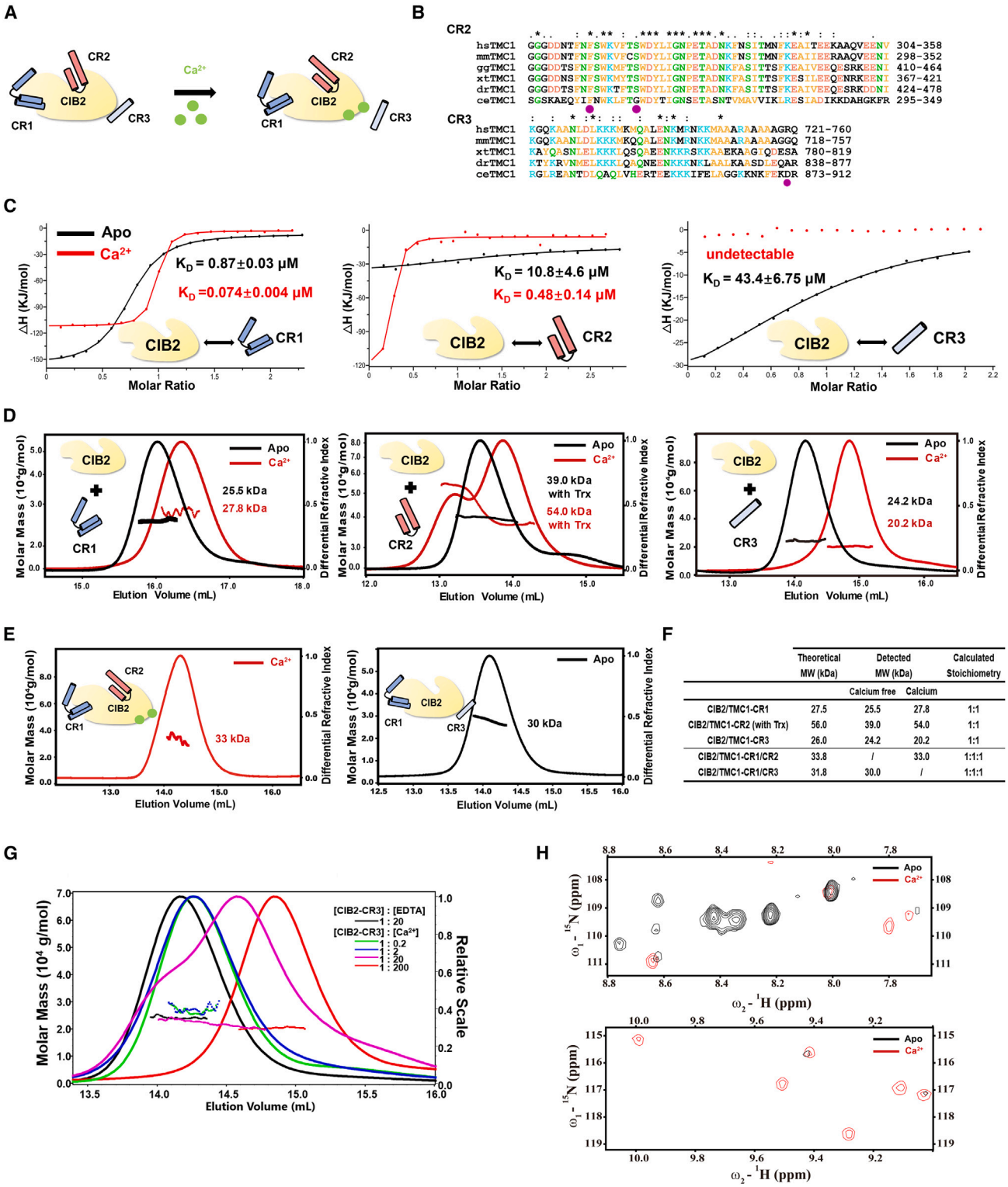

	Theoretical MW (kDa)	Detected MW (kDa)		Calculated Stoichiometry
		Calcium free	Calcium	
CIB2/TMC1-CR1	27.5	25.5	27.8	1:1
CIB2/TMC1-CR2 (with Trx)	56.0	39.0	54.0	1:1
CIB2/TMC1-CR3	26.0	24.2	20.2	1:1
CIB2/TMC1-CR1/CR2	33.8	/	33.0	1:1:1
CIB2/TMC1-CR1/CR3	31.8	30.0	/	1:1:1

Figure 2. CIB2 interacts with CR1, CR2, and CR3 of TMC1, regulated by calcium

(A) Schematic diagrams show the interaction between CIB2 and three CRs of TMC1 and the conformational change of the complex after CIB2 binding Ca^{2+}.

(B) Sequence alignments of TMC1 CR2 and TMC1 CR3 from different species. Conserved residues are colored orange (nonpolar), green (polar), blue (positive charged), and red (negative charged). The dominant disease mutation sites are indicated with purple circles. hs, *Homo sapiens*; mm, *Mus musculus*; gg, *Gallus gallus*; xt, *Xenopus tropicalis*; dr, *Danio rerio*; ce, *Caenorhabditis elegans*.

(legend continued on next page)

Furthermore, the dissociation process of TMC1 CR3 from CIB2 was elucidated through Ca^{2+}-titration SEC-MALS experiments (Figure 2G). The CIB2-TMC1 CR3 complex gradually disassembled with increasing Ca^{2+} concentrations, initiating at a molar ratio of 1:20 and fully dissociated at a ratio of 1:200. Despite some variation in the precise calculation (~3.5[60] channels per stereocilium or ~8 at the apex to ~20 at base[61]) regarding the exact number, a remarkably small quantity of TMC1 molecules was found at the tip of stereocilia. Considering the EC Ca^{2+} concentrations as 20 μM[51,62] (estimated as 220:1 for [Ca^{2+}]:[TMC1]) beneath the membrane, TMC1 CR3 has enough calcium sensitivity for the dissociation upon Ca^{2+} influx after the channel opens. To further validate the conformational changes induced by calcium in the CIB2-CR1 complex, NMR-based titration experiments were conducted (Figure 2H). In the *apo* state, significant ^{1}H-^{15}N HSQC signals of CIB2 and TMC1-CR1 complex were observed at ω_2-^{1}H 8.0–8.8; these signals vanished upon Ca^{2+} binding to CIB2, demonstrating the exquisite sensitivity of NMR chemical shifts to Ca^{2+} binding. Meanwhile, in the Ca^{2+}-bound state of the complex, residues show signals at ω_2-^{1}H 9.0–10.0, indicating conformational changes in the complex as a result of Ca^{2+} binding. To further consolidate the calcium-sensing ability of the TMC1-CIB2 complex, we assessed their preference for divalent ions. Our ITC experiments showed that CIB2 has a binding affinity of ~3.43 μM for Ca^{2+}, but no significant binding to Mg^{2+} (Figure S2A). The opposite conclusion compared with previous report[63] may be attributed to the adoption of different experimental methods. Additionally, we identified the interaction of CIB2 and CR3 under Mg^{2+} state, which showed a comparable binding affinity to the *apo* state (Figure S2B). Inductively coupled plasma-mass spectrometry (ICP-MS) analysis showed that TMC1 CR1 and CIB2 complex binds to five times more Ca^{2+} than Mg^{2+} under cellular concentrations (10:1 ratio of Mg^{2+} to Ca^{2+}, Figure S2C).

In summary, we identified a vertebrate-specific binding site on TMC1, named CR3, that interacts with *apo* CIB2. In addition, Ca^{2+} regulates the binding between CIB2 and TMC1 CRs by modulating CR1 and CR2 interactions and dissociating CR3 (Figure 2A). To better understand how Ca^{2+} mediates MET channel function, we moved on to elucidate the calcium regulation on the complex of CIB2 and the full-length TMC1.

The assembly of the mammalian full-length TMC1-CIB2 complex

Combining the complex structures of mammalian TMC1 CR1-CIB2 (Figure 1B) and TMC1 CR2-CIB3 (PDB: 6WUD),[30] biochemical characterization on the Ca^{2+}-regulated association between TMC1 and CIB2 (Figure 2), and the previous studies on TMC1 TM regions that TMC1 assembles as a dimer and resembles TMEM16 ion channels,[19] we can assemble a structural model of the mammalian TMC1 and CIB2 complex using AlphaFold-Multimer (Figure 3A). First, the interaction between CIB2 and full-length TMC1 was verified by co-immunoprecipitation (coIP) experiments. We found that the deletion of individual CR domains reduced the CIB2-TMC1 interaction in the absence of Ca^{2+} (Figure S3A). However, even with both CR1 and CR2 deleted, CR3 still interacted with CIB2 in the absence of Ca^{2+}, indicating that TMC1-CR3 is involved in the *apo* state of the complex (Figure S3B).

The structure model of the human TMC1 dimer was obtained using the deep-learning-based protein-protein interaction predictor AlphaFold-Multimer with default settings for model parameters and the selection of a complete genetic database.[64] The predictions were ranked based on a model confidence metric, a weighted combination of predicted TM-score (pTM) and interface pTM. The whole structure of the TMC1-CIB2 dimer (Figure 3A) was constructed by aligning the TMC1 and CIB2 onto the structure of CIB3-TMC1 CR2 (PDB: 6WUD) and substituting the TMC1 CR1 segment (amino acids 81–130) by the corresponding counterpart in our crystal structure of CIB2-CR1. The preparation of molecular dynamics (MD) input files of the TMC1-CIB2 dimer was conducted through the bilayer builder of CHARMM-GUI.[65] The protein complex with the membrane was employed as the starting point for the following all-atom MD simulations, which were performed using the GROMACS program[66] and CHARMM36 force field.[67]

As displayed in Figure 3A, the structure of the TMC1-CIB2 dimer exhibits a symmetric conformation between two monomers, which are formed with the mediation of the TM10 and the CR3 helices (Figure 3A). CR1 (at the N-terminal of TM1) and CR2 (between TM2 and TM3) of TMC1 embrace the CIB2 protein in the intracellular region, and calcium ions bind to the EF-hand 3 and 4 in CIB2 (Figure 3A). The cytoplasmic part provides sufficient space for the simultaneous binding of CR1 and CR2 with CIB2 in the calcium-bound state. The putative pore of TMC1, characterized in the previous study,[19] is formed by TM4-8.

We then performed a structural superimposition of the human TMC1-CIB2 complex model with the recently reported *C. elegans* TMC1/CALM1/TMIE complex[42] (Figure 3B) and TMC2/CALM1/TMIE complex structures[43] (Figure 3C). The overall dimer conformation and TM region topology show similarity among the three complexes (Figure 3D). All the TM regions of ceTMC1, ceTMC2, and the hsTMC1 protomer are composed of ten helices (Figure 3E). However, significant variations are observed in the CRs, especially in CR1 and CR3, which are responsible for CIB2 association confirmed by our biochemical data. Our structure shows that CR1 of human TMC1 consists

(C) ITC analysis shows that CIB2 binds to TMC1 in three CRs with different binding affinity in *apo* (black) and Ca^{2+} (red) states. 10 mM ethylenediaminetetraacetic acid (EDTA)/$CaCl_2$ were added in buffer. See also Figure S7A.
(D) SEC-MALS analysis of CIB2 binds to TMC1 CR1/CR2/CR3 in *apo* (black) and Ca^{2+} (red) states. Trx, thioredoxin.
(E) SEC-MALS analysis of CIB2 with TMC1 CR1and TMC1 CR2 in Ca^{2+} state (red) and TMC1 CR1 and TMC1 CR3 in *apo* state (black).
(F) A summary of SEC-MALS results, showing the molecular weight and calculated stoichiometry.
(G) The SEC-MALS analysis of calcium titration to the TMC1 CR3 and CIB2 complex. The varied CIB2-CR3 complex to Ca^{2+} molar ratio was shown in different colors (black, green, purple, blue, and red).
(H) An overlay plot of a selected region of ^{1}H-^{15}N HSQC spectrum of CIB2 and TMC1-CR1 complex. The *apo* state is showing in black, and Ca^{2+} state is showing in red. 10 mM EDTA/$CaCl_2$ were added in buffer. ppm, parts per million.

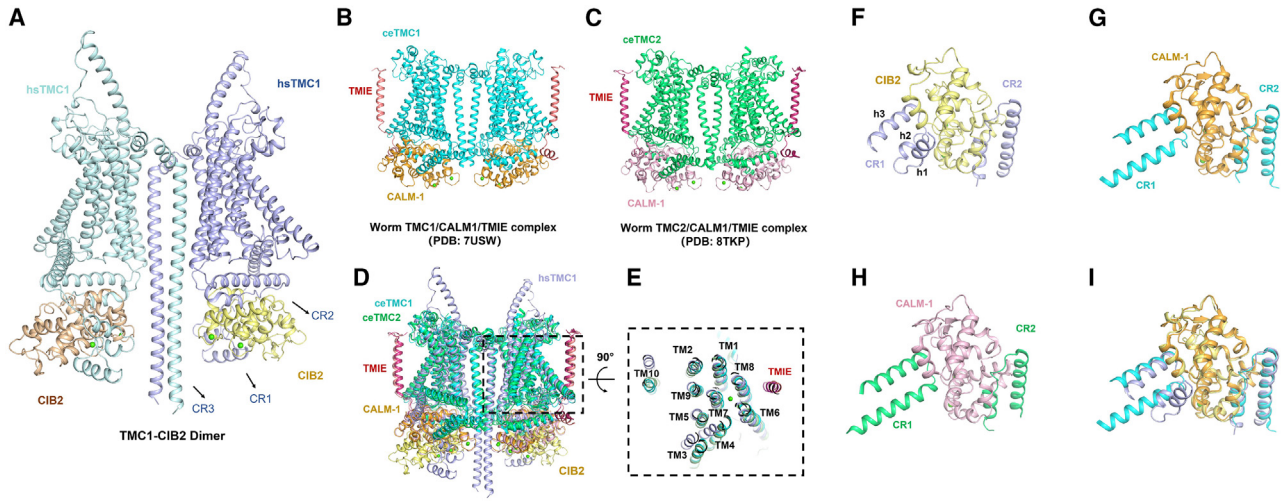

Figure 3. The assembly of the mammalian TMC1-CIB2 complex

(A) The structure model of TMC1-CIB2 dimer. TMC1 CR1/2/3 and CIB2 are labeled. The calcium ions are shown as green spheres.

(B) The complex structure of *C. elegans* TMC1/CALM-1/TMIE (PDB: 7USW).

(C) The complex structure of *C. elegans* TMC2/CALM-1/TMIE (PDB: 8TKP).

(D) Superimposition of *C. elegans* TMC1 complex, TMC2 complex and human TMC1-CIB2 complex model.

(E) The top-down view of the superimposition of the transmembrane regions of *C. elegans* TMC1, TMC2 complexes, and human TMC1-CIB2 complex model.

(F–I) Local structural comparison of the human TMC1 CR1/CR2 complexed with CIB2 (F), *C. elegans* TMC1 cytoplasmic regions (CR1 and CR2) complexed with CALM1 (G), and *C. elegans* TMC2 cytoplasmic regions (CR1 and CR2) complexed with CALM1 (H).

of three short α helices (h1–h3), with h1 being absent in the worm TMC1 and TMC2 structures and sequences (Figures 3F–3I). On the other hand, the conformation of CR2 is conserved, folding into two α helices and making contact with a hydrophobic trench at the C-terminal of CIB2/CALM (Figures 3F–3I). The other notable difference lies in CR3 region, which forms a long helix extending from the TM10 helix in our complex structure model, but it is completely absent in both worm structures (Figure 3E).

The conformational change of full-length TMC1-CIB2 complex in response to Ca^{2+}

To understand the molecular dynamic behavior of full-length TMC1-CIB2 complex under the regulation by Ca^{2+}, a customized MD-based simulation workflow was designed accordingly. The simulations were performed on the two conformational states of the TMC1-CIB2 complex, i.e., the *apo* state without Ca^{2+} and the Ca^{2+} bound *holo* state. For simulation of the Ca^{2+} state (Figure S4A), the complex was equilibrated in a cubic box filled with TIP3P[68] water molecules, some of which were replaced by sodium and chloride ions. Subsequently, energy minimization, NVT (constant substance, volume and temperature), and NPT (constant substance, pressure and temperature) equilibrations were conducted sequentially to stabilize the temperature and pressure of the system to 310 K and 1 bar, respectively. Finally, MD simulation was performed on the equilibrated structure for 300 ns under the NPT ensemble as in previous reports.[69,70] To simulate the *apo* state (Figure S4B), we used two different strategies, changing the membrane tension and the membrane thickness, respectively, to mimic the mechanical signal. A more decisive design is to remove calcium ions to monitor the dynamic behavior based on our findings of calcium modulation. The following analyses were conducted on the most representative structure (center structure of a cluster) clustered from MD trajectories.

Detailed structural analysis revealed the following conformational change between the two states. First, in the MD-derived structure of TMC1-CIB2 Ca^{2+} form, the CR3 segment of TMC1 is away from CIB2, which is consistent with our biochemical results that no detectable binding between CR3 and Ca^{2+}-CIB2. The Ca^{2+} binding involves the residues of D116, N118, D120, D127, D157, D159, D161, and D168 in CIB2 (Figure S4A). In the *apo* state with membrane tension change, the CR3 region bends toward CIB2, thus forming multiple salt bridges (R759-D120, R759-D161, K746-D159, K742-D157, K742-D168, R744-E170, and R744-D171) with residues within and around the previous Ca^{2+}-binding sites (Figure S4B). Meanwhile, we also used another strategy to do *apo* state simulation with a thinner membrane, which is used in simulating the opening process of MscL channel.[71] The electrostatic interactions formed between CR3 and CIB2 were also observed in the structure derived from the simulation (Figure S4C). This provides the structural basis for the Ca^{2+}-mediated modulation of the TMC1-CIB2 complex. Consistently, the ITC results showed that although single mutations of Lys/Arg to Ala have only minor effects, the triple substitutions of the positively charged residues with Ala in CR3 significantly reduce its binding affinity with CIB2 (Figures S4D and S7E).

Disruption of the Ca^{2+}-binding element perturbs the channel performance *ex vivo*

To consolidate our hypothesis, we conducted a series of mutagenesis experiments to assess whether the Ca^{2+}-binding sites of CIB2 are essential for the proper function of MET. It is worth mentioning that MET was unaffected in *Cib2* knockout vestibular

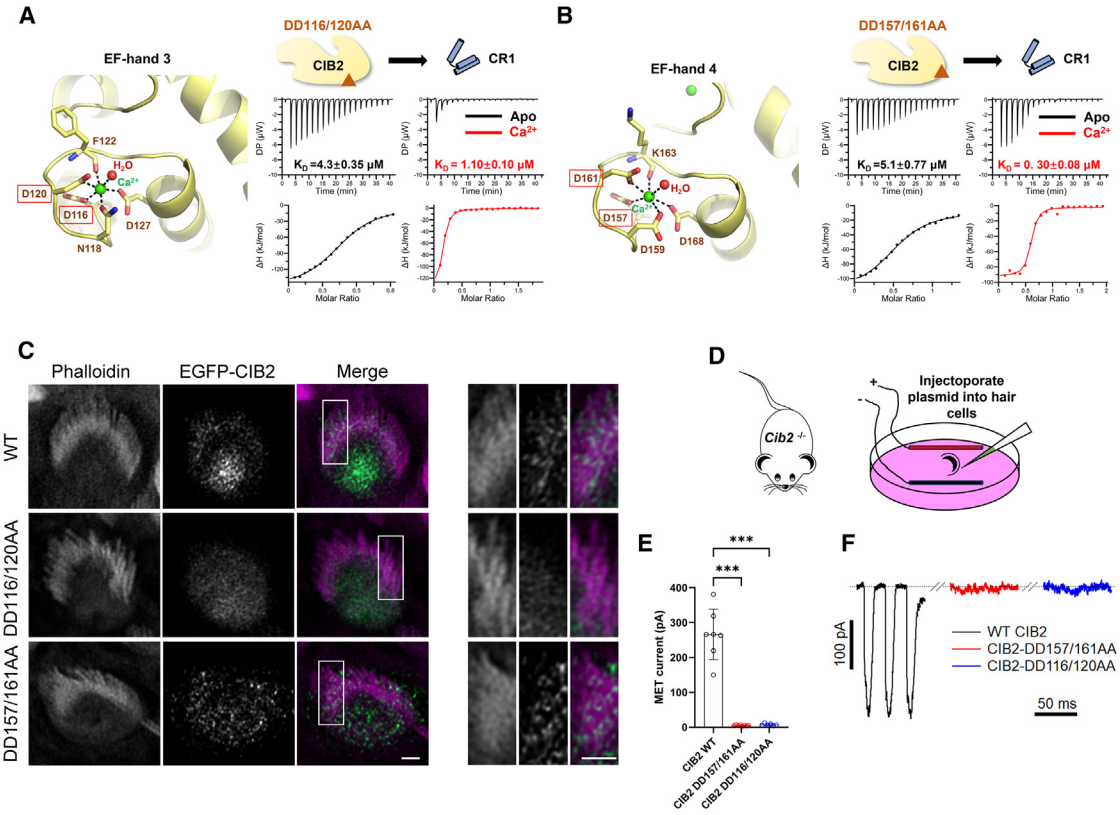

Figure 4. Calcium-binding mutations in EF3 and EF4 of CIB2 affect MET in mice OHCs

(A and B) The structural details of EF-hand 3 and EF-hand 4 (left) and ITC results of double-mutant residues of CIB2 interacting with CR1. The mutant residues are framed in red; the calcium ions are colored in green. ITC results are shown in apo state (black) and Ca^{2+} state (red), respectively.

(C) Representative OHCs from wild-type mice injectoporated with the indicated constructs, visualized in grayscale and merged for CIB2 (green) and phalloidin (magenta). Higher magnification views of the boxed areas in the merged images are shown on the right. Scale bar, 1 μm.

(D) A schematic drawing of injectoporation procedure to express genes in hair cells.

(E) Quantification of the MET current amplitudes from recordings in P3 *Cib2*$^{-/-}$ OHCs injectoporated with different CIB2 constructs as indicated. Data are shown as means ± SEM; ***$p < 0.001$. *n* (CIB2 WT) = 6, *n* (CIB2 DD157/161AA) = 8, *n* (CIB2 DD116/120AA) = 7.

(F) Representative examples of MET currents recorded from OHCs in *Cib2*$^{-/-}$ mice injectoporated with different CIB2 constructs as indicated.

hair cells (VHCs), and CIB3 could compensate for the loss of CIB2 in VHCs.[31] In agreement with previous reports,[30,72] structural analysis of the mammalian CIB2-TMC1 CR1 complex structure revealed that EF-hand 3 and EF-hand 4 of CIB2 each bind one Ca^{2+} ion. In EF-hand 3, D116, N118, D120, F122, and D127 participate in Ca^{2+} coordination (Figure 4A); in EF-hand 4, D157, D159, D161, K163, and D168 interact with the second Ca^{2+} ion (Figure 4B). It is assumed that substituting D116 and D120 on EF-hand 3 and D157 and D161 on EF-hand 4 with alanine should disrupt Ca^{2+} coordination. We first verified the direct impairment of both double mutants in their binding to Ca^{2+}, resulting in a ~25-fold decrease for DD116/120AA and a ~12-fold decrease for DD157/161AA compared with CIB2 wild type (WT) (Figure S5A). The ITC experiments further showed that both double mutants impair their binding with TMC1 CR1 in response to Ca^{2+} (~150-fold decrease for DD116/120AA in Figures 2C and 4A and ~50-fold decrease for DD157/161AA in Figures 2C and 4B). Additionally, the indicated mutations of CIB2 exhibit effects on its binding to CR2 and CR3 (Figures S5B and S5C). These results suggested that the Ca^{2+}-binding elements on CIB2 were essential for the interaction with TMC1.

We injectoporated WT CIB2 as well as two mutants, DD116/120AA and DD157/161AA, into WT mouse cochleae (Figure 4C). Immunostaining results demonstrated that CIB2-DD157/161AA localized to the stereocilia, similar to CIB2-WT (Figure 4C). In contrast, CIB2-DD116/120AA exhibited impaired protein trafficking and localized mainly in the cell body (Figure 4C). Consistent results can also be observed in Figure S5D. Given the approximately 25-fold decrease in binding affinity of CIB2-DD116/120AA for Ca^{2+} (Figure S5A), this result indicates that defective calcium binding of EF-hand 3 led to protein mislocalization of CIB2.

We further performed MET current rescue experiments on *Cib2* knockout mice. We recorded the MET current in *Cib2*$^{-/-}$ mice injectoporated with different CIB2 constructs (Figure 4D). CIB2-WT successfully restored the MET current in P3 *Cib2*-deficient outer hair cells (OHCs). In contrast, no MET current was detected in CIB2-DD116/120AA or CIB2-DD157/161AA overexpressing *Cib2*-deficient OHCs (Figure 4E), despite CIB2-DD157/161AA can localize to stereocilia. Representative examples of

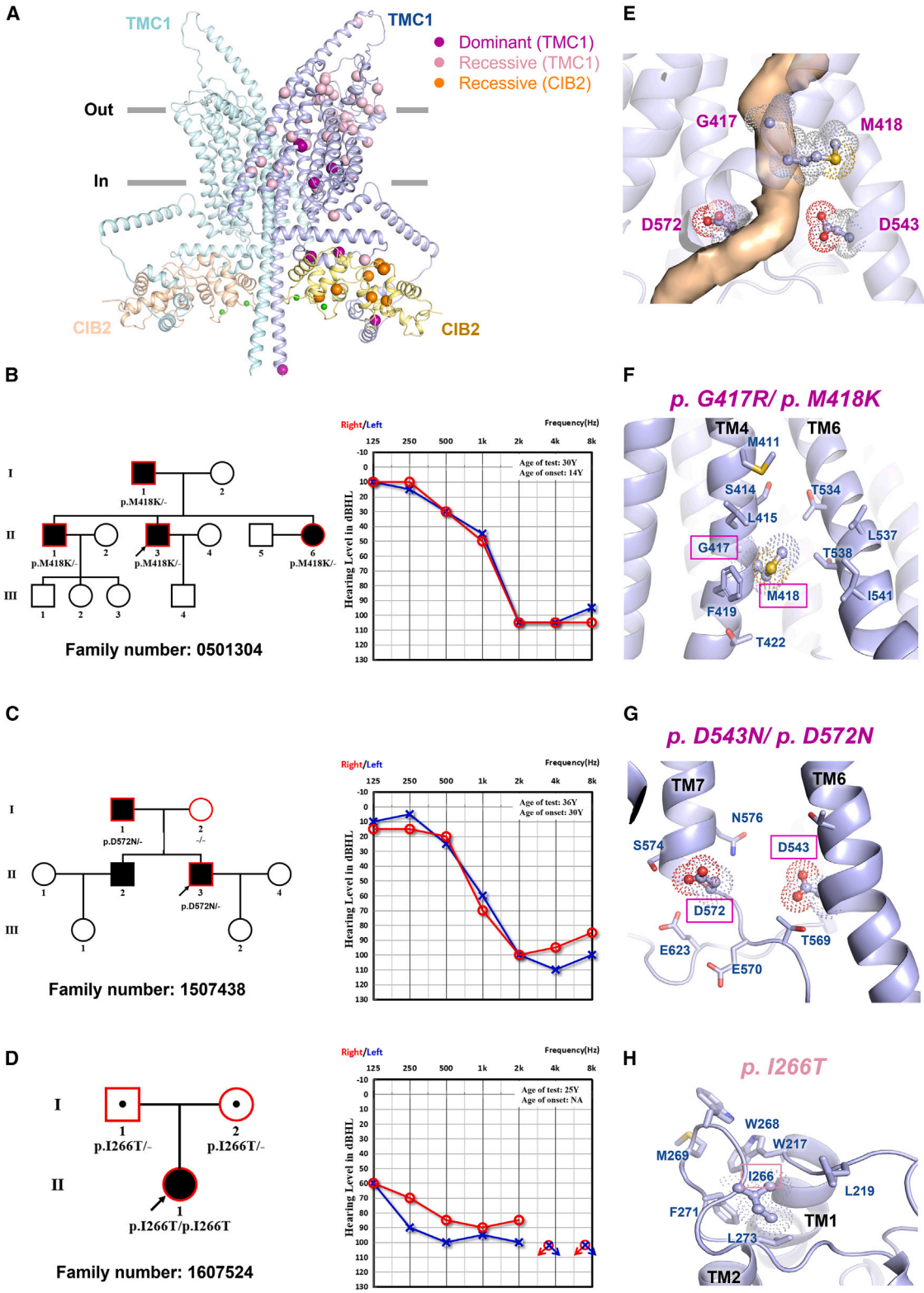

Figure 5. The autosomal dominant hearing loss mutations of TMC1 around the putative pore of the MET

(A) The locations of disease mutations were mapped onto the structure model of TMC1-CIB2.

(B–D) Left: the pedigrees of families 0501304 and 1507438 with autosomal dominant inheritance pattern (M418K and D572N), and family 1607524 with autosomal recessive inheritance pattern (I266T). The arrows pointed to the probands, and the family members with genetic testing were framed in red; Right: audiological

(legend continued on next page)

MET currents recorded from OHCs are shown in Figure 4F. These *ex vivo* experiments confirmed the significance of Ca^{2+}-binding elements on CIB2 by regulating its interaction with TMC1.

The autosomal dominant hearing loss mutations of TMC1 cluster around the putative pore

Variants in *TMC1* have been associated with both autosomal recessive and autosomal dominant hearing loss (DFNA36 and DFNB7/11). More than 100 different DFNB7/11 variants and 8 DFNA36 variants have been identified (Table S3, combination of reported variants and families recruited in this study). This genetic heterogeneity poses a significant challenge for accurate diagnosis and effective treatment. However, our comprehensive characterization of the TMC1-CIB2 complex (Figure 5A) has enabled us to match these different clinical phenotypes with the underlying pathogenesis at a molecular level.

This study recruited three hearing loss families to reinforce the evidence of the genetic heterogeneity of *TMC1*. The *TMC1* pathogenic mutations were confirmed and co-segregated in all three families. Family 0501304 (p.M418K) and 1507438 (p.D572N) showed an autosomal dominant inheritance pattern (Figures 5B and 5C), and family 1607524 (p.I266T) showed an autosomal recessive inheritance pattern (Figure 5D). Patients in family 0501304 (p.M418K) and 1507438 (p.D572N) showed a late-onset bilateral sensorineural severe hearing loss, mainly affecting high frequencies. The patient in family 1607524 (p.I266T) showed an early-onset bilateral profound sensorineural hearing loss in which all frequencies were affected.

The total of 51 missense variants (43 in TMC1 and 8 in CIB2) were mapped onto the complex structure of mammalian TMC1-CIB2 (Figure 5A; Tables S2 and S3). Truncation/deletion mutations are not discussed here as these can be interpreted as null mutations. Among the 43 TMC1 mutation site, 14 are located in the EC region, 24 in the TM region, and 5 in the cytosolic (Cyto) region (Figure 5A; Table S3). For the mutants in the EC region, further investigation is needed to determine the involvement of binding to other components of MET.

Interestingly, all of the pore-region mutants are linked to autosomal dominant hearing loss. Four of the 24 TM variants occur in the putative pore of TMC1 (G417R and M418K in TM4, D543N in TM6, and D572N in TM7) (Figure 5E). These disease-causing mutations in this category are likely to impact the conductivity of the putative pore of TMC1. As shown in Figure 5F, p.G417 and p.M418 are neighbors in TM4 of TMC1. Substituting Gly417 with Arg and Met418 with Lys is expected to disrupt the hydrophobic networks formed by the surrounding residues and introduce positively charged residues that are unfavorable for Ca^{2+} permeation through the channel pore (Figure 5F). The other two dominant mutations, p.D543N in TM6 and p.D572N in TM7, are located near the cytosolic end of the putative channel pore. Substituting Asp with Asn would remove the negatively charged residue, which is critical for binding Ca^{2+} (Figure 5G). Previous studies have shown that equivalent mutations of M418K in mouse (p.M412K) decreases Ca^{2+} permeability and D569N in mouse (equivalent to p.D572N in human) diminished the influx of Ca^{2+}.[41] Moreover, p.D572N in human TMC1 disrupted LHFPL5 binding and destabilized TMC1 expression.[73] The recessive mutation p.I266T lies at the EC loop between TM1 and TM2 and forms extensive hydrophobic interactions with W217, L219, W268, M269, F271, and L273. Substitution of Ile with Thr may influence these hydrophobic interactions (Figure 5H) and result in a recessive phenotype.

Hearing-loss-related mutations disturb TMC1-CIB2 interaction

Notably, the remaining dominant mutations (p.M113I, p.F313S, p.S320R, and p.R759H) in TMC1 are in the binding regions with CIB2 (Figure 6A), suggesting the interaction of TMC1 and CIB2 plays critical roles in MET. As mentioned above (Figure 1E), M113 (equivalent to M107 in mouse) at CR1 directly participates in binding with CIB2, and its sidechain inserts into the hydrophobic groove formed by Y16, C19, and V92 of CIB2. The groove would not accommodate the substitution of Met with Ile (Figure 6C). p.F313S and p.S320R (equivalent to p.F307 and p.S314 in mouse), located at the binding interface of CR2 and CIB2, are expected to destabilize the hydrophobic contacts formed by F313, F318, W321, I338, F342, and I346 from TMC1 and F70, Y115, L135, and V148 from CIB2, thus impairing the interaction of TMC1 CR2 and CIB2 (Figure 6D). As expected, these mutations all weakened or even abolished the TMC1-CIB2 interaction in ITC-based assays (Figures 6B and S7D).

The p.R759H missense mutation resides at the C-terminal end of TMC1 CR3. According to the MD-derived model of TMC1-CIB2 *apo* form, the two R759 residues from the TMC1 dimer form salt bridges with the residues for Ca^{2+} coordination in CIB2 (i.e., $D120^{EF3}$, $E126^{EF3}$, and $D161^{EF4}$) (Figure 6E). Substitution of Arg759 with His is expected to interfere with the salt bridges' formation, further destabilizing the binding of CR3 and CIB2. Family 1607556 (p.R759H) indeed showed an autosomal dominant inheritance pattern (Figure 6F), and the patient showed an early-onset bilateral profound sensorineural hearing loss at 2 years old, mainly affecting middle frequencies (Figure 6G). The discovery of a human mutation on the binding interface of TMC CR3-CIB2 reinforces our model, highlighting the pathophysiological significance of the CR3-binding site.

Eight deafness mutations in CIB2 have been identified until now (Figure S6A). To further explore the effects of the mutations on CIB2-TMC1 binding, we picked up four mutations (p.E64D, p.R88W, p.F91S, and p.I123T) and performed ITC assays. Unsurprisingly, all four CIB2 mutations showed decreased binding affinities with TMC1 CR1 or CR3 (Figure S6F). The structural analysis allows us to rationalize the structural effects of these mutations. E64D missense mutation is located at the h3 helix and forms salt bridges with R33 located at the h2 helix of CIB2; therefore, a lack of methyl might weaken the interaction

phenotypes of deafness patients with pure tone audiograms of the probands. The red represents the hearing of the right ears, and the blue represents the left ears; symbols "o" and "x" denote air conduction pure tone thresholds at different frequencies in the right and left ears. dB, decibels; Hz, hertz; Y, years old.
(E) The structural details of the putative pore of TMC1.
(F–H) Structure analysis on the dominant variants (framed in purple) and recessive variants (framed in pink). Residues involved in protein interaction are shown with a stick model, and variants residues are shown as dots.

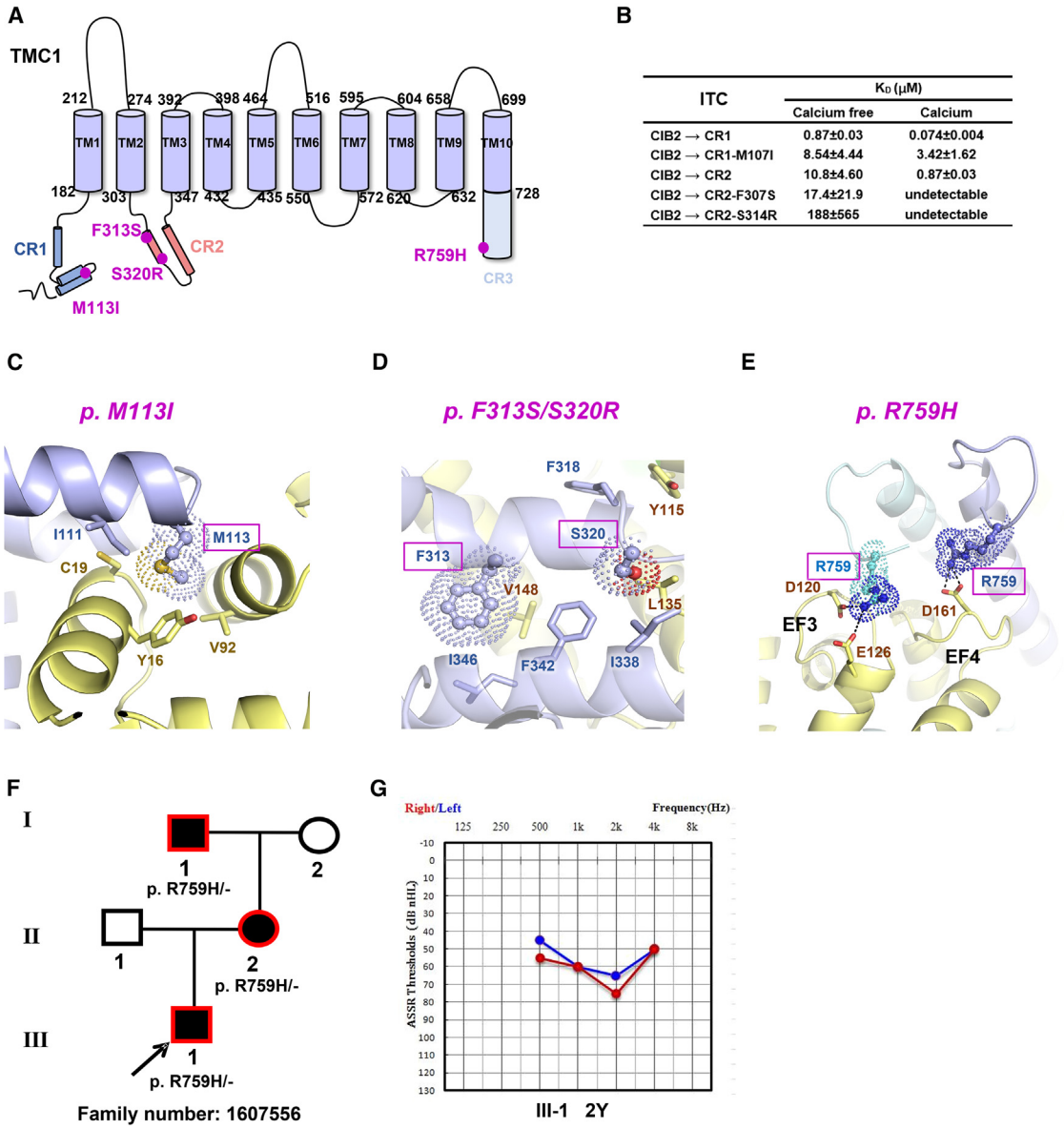

ITC	K_D (μM)	
	Calcium free	Calcium
CIB2 → CR1	0.87±0.03	0.074±0.004
CIB2 → CR1-M107I	8.54±4.44	3.42±1.62
CIB2 → CR2	10.8±4.60	0.87±0.03
CIB2 → CR2-F307S	17.4±21.9	undetectable
CIB2 → CR2-S314R	188±565	undetectable

Figure 6. Dominant mutations on the CRs of TMC1

(A) A domain diagram of TMC1 with labeled dominant disease mutations colored in purple.

(B) A table summarizes the ITC results of CIB2 interacting with variants of TMC1. See also Figure S7D.

(C–E) The structural details of the dominant variants of TMC1 interacting with CIB2. Dominant variants are framed in purple and shown as dots, and residues involved in protein interaction are shown with a stick model.

(F) The pedigree of the family 1607556 with autosomal dominant inheritance pattern. The arrows pointed to the probands, and the family members with genetic testing were framed in red.

(G) Auditory steady-state response (ASSR) hearing threshold of the probands tested at 2 years old. The red represents the hearing of the right ears, and the blue represents the left ears. dB, decibels; Hz, hertz; Y, years old.

and destabilize the folding of CIB2 (Figure S6B). The F91S missense mutation, located at the h5 helix of CIB2, is expected to interfere with the hydrophobic contacts among L30, F34, L37, M62, F88, F91, V92, and F95, thus destabilizing the folding of CIB2 (Figure S6C). Similarly, p.I123T near the Ca^{2+} binding site might also impair the surrounding hydrophobic networks (Figure S6D). The mutation R66W occurred on the hydrophilic loop between h3 and h4 and is close to another deafness mutation site R186W in three-dimensional space (Figure S6E). Given that the sidechains of Arg88 and Arg186 are exposed to solvent, the substitutions of Arg with the large hydrophobic sidechain of Trp are speculated to destabilize the protein (Figure S6E). Furthermore, it has been recently reported that R186W mutant significantly slows down MET channel activation and causes loss of membrane-shaping protein BAIAP2L2 localization at the lower tips of stereocilia.[74] Although these mutations are not

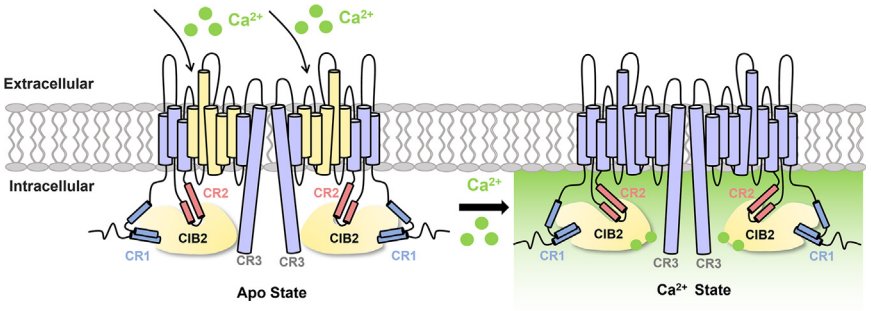

Figure 7. The model of Ca^{2+} mediating the TMC1-CIB2 complex

In this model, TMC1 dimers are shown in purple, with the putative ion pore highlighted in yellow. CIB2 proteins are depicted in yellow, associated with the TMC1 CR1/2/3. Calcium influx is represented as an increasing gradient in green, indicating its potential role in the auditory process.

directly involved in interacting with TMC1, they might impair the overall conformation of CIB2, thus interfering with its binding capacity.

In summary, four dominant variants of TMC1 cluster around the putative ion channel pore, while others are located in the CRs responsible for binding with CIB2. With the structural and biochemical analyses on the variants and investigation on the pedigrees and audiological phenotypes of deafness patients, we have revealed this genotype—structype—phenotype correlation. This understanding can facilitate accurate diagnosis and tailored treatment options for individuals affected by TMC1-related hearing loss.

DISCUSSION

Our study shows that the TMC1-CIB2 complex undergoes a Ca^{2+}-induced conformational change, highlighting the crucial role of Ca^{2+}-binding elements of CIB2. In addition to the previously identified TMC CR1 binding to CIB2[29] and the reported complex structure of TMC1 CR2-CIB3,[30] we identified a new binding site on TMC1, named CR3, that only interacts with *apo* CIB2. Notably, the TMC1 CR3 region is conserved only among vertebrates, coinciding with the emergence of the inner ear. Our findings suggest that the CR3 binding is also pathophysiological critical, as human mutations on the binding interface are linked to hearing loss (Figures 6E–6G).

We assembled a full-length mammalian TMC1-CIB2 complex, using AlphaFold-Multimer and our high-resolution TMC1 CR1-CIB2 structure. Based on this model, we further developed a customized MD-based simulation workflow to examine the molecular dynamic behavior of the TMC1-CIB2 with/without Ca^{2+}, suggesting that the complex undergoes a Ca^{2+}-induced conformational change (Figures 2A, 7, and S3A), which was further supported by the *ex vivo* organotypic cochlea model (Figure 4) and clinical genetic data (Figures 5 and 6).

EF-hand proteins in sensory systems

The EF-hand motif is a common calcium-sensing motif, participating in various physiological processes. The classical EF-hand is a helix-loop-helix motif, with the loop region accommodating calcium. Calmodulin is the most famous EF-hand protein, which serves as the Ca^{2+} sensor for several voltage-gated sodium and calcium channels. At elevated cytosolic Ca^{2+} levels (caused by channel opening), Ca^{2+}-bound calmodulin changes its binding mode with the calcium channel and inactivates the channel rapidly. TRP (transient receptor potential) channels generally act as molecular sensors of multiple stimuli, ranging from changes in pH, chemical agents, and temperature. TRPs are unique by including the EF-hand region in its cytosolic sequence instead of interacting with other EF-hand-containing proteins. CIB2, just like calmodulin, has four EF-hands, with two capable of binding calcium. Here, we propose a model for Ca^{2+} regulation of the TMC1-CIB2 complex: in the *apo* state/Mg^{2+} state, CIB2 binds to CR1, CR2, and CR3 of TMC1 (Figures 2E, 2G, 7, S2B, and S3). Upon Ca^{2+} influx, CIB2 dissociates from CR3, triggering a conformational change of TMC1-CIB2 complex that also involves CR1 and CR2 (Figures 2E, 2G, 7, and S3). Unlike other mechanosensitive channels, the auditory MET channel exhibits ultrafast open-close kinetics in response (microsecond) to fluctuating sound inputs. With its high diffusion rate, Ca^{2+} ions play a crucial role in various rapid regulatory processes. Our study supports the hypothesis that CIB2-TMC1 may be involved in Ca^{2+}-mediated MET complex conformation remodeling for sound transduction, warranting further investigation.

It is recognized that Ca^{2+} plays a crucial role as a regulator in MET kinetics. The influx of Ca^{2+} can modulate the activation and adaptation of the transducer current in a concentration-dependent manner.[45,46] However, the involvement of calcium in fast adaption of MET remains under debate.[48–50] The Ca^{2+}-dependent binding of TMC1-CIB2 may lay a foundation for fast/slow reactions of the transduction (tens or even hundreds of kilohertz). Further research is needed to elucidate the mechanisms underlying the modulation of the MET channel across different timescales.

Linking genotype, structype (structure type), and clinic phenotype together

The issue of genetic heterogeneity has long posed a challenge in clinical diagnosis, particularly in non-syndromic hereditary hearing loss, which has a high degree of genetic heterogeneity, especially for *TMC1* with dominant and recessive inheritance patterns. Depending on the positions on the protein structure and the physicochemical properties of the substituted amino acid, variants can affect the proper function of the protein in different ways. For the recessive mutations, the disturbance caused by the amino acid change can be compensated by the WT copy. However, some variants can be severe and have a dominant-negative effect. In that case, one copy of the substation is enough to cause the phenotype as an autosomal dominant disease. Autosomal recessive hearing loss (DFNB7/11) and autosomal dominant (DFNA36) are like the two faces of *TMC1*.

To date, over 100 pathogenic variants in TMC1 have been reported,[75,76] with only 8 of them responsible for DFNA36 (M113I, F313S, S320R, G417R, M418K, D543N, D572N, and R759H). However, the mechanism by which the dominant and recessive mutations lead to abnormal TMC1 function and regulation remains mostly unexamined. We collected 43 missense mutations of hearing loss patients from online databases as well as clinic data and mapped these mutation sites on the TMC1-CIB2 complex structure model (Figure 5A). We systematically characterized the deafness mutations by combining structural analysis, biochemical validation, *ex vivo* assays, and genetic studies, thoroughly investigating the clinical phenotypes of hearing loss from micro to macro (Figures 5, 6, and S6). Four of the eight dominant mutation sites cluster around the ion pore, while the other four are responsible for binding with CIB2. Mutations near the putative ion pore are likely to interfere with calcium binding and gating, which are critical for the mechanotransduction process. Similarly, mutations affecting CIB2 binding can disrupt TMC1's interaction with CIB2, implying a potential role for CIB2 in regulating the MET channel. Disrupting this interaction could affect channel gating or lead to protein mislocalization, potentially resulting in dominant-negative effects. In contrast, recessive mutations may result in a loss of function that only manifests when both alleles are mutated, as one functional allele is typically sufficient to maintain normal protein function. In our structural analysis, many recessive mutations are located in the hydrophobic core, where they tend to disrupt the overall folding and stability of TMC1. Since TMC1 functions as part of a multimeric complex, loss of function due to folding defects can often be compensated by the remaining functional copies of the protein. This provides a molecular level explanation for the genetic heterogeneity of *TMC1* in hearing loss, highlighting how structural differences contribute to the functional variability observed in individuals.

Limitations of the study

Our study demonstrates that the TMC1-CIB2 complex undergoes a Ca^{2+}-induced conformational change, highlighting the significance of Ca^{2+}-binding elements in CIB2. This was achieved through a combination of *in vitro*, *ex vivo*, and *in silico* methods. Further studies on the structures of full-length mammalian MET complex under various conditions will significantly enhance our understanding of how MET functions in hearing.

RESOURCE AVAILABILITY

Lead contact

Any information and requests for resources and reagents should be directed to and will be fulfilled by the lead contact, Qing Lu (luqing67@sjtu.edu.cn).

Materials availability

All reagents generated in this paper are available upon request to the lead contact.

Data and code availability

- Original data reported in this paper will be shared by the lead contact upon request.
- The atomic coordinate of the complex of TMC1 CR1 and CIB2 has been deposited to the Protein Data Bank under the accession codes: 8Z3F.
- This study did not generate any code.

ACKNOWLEDGMENTS

We thank staff members of the BL19U1 beamline of the National Facility for Protein Science Shanghai (NFPS) at Shanghai Synchrotron Radiation Facility and Shijing Huang for X-ray diffraction data collection. We thank the staff members of the Large-Scale Protein Preparation System and the nuclear magnetic resonance system of NFPS, Shanghai Advanced Research Institute, Chinese Academy of Sciences, China, for providing technical support and assistance in data collection and analysis. We thank Ulrich Müller for his comments and for improving our manuscript. We thank Ruoxu Gu from Shanghai Jiao Tong University for his suggestions on MD simulation design. We thank Yuyu Guo and Haiyan Yu from the core facilities for life and environmental sciences, Shandong University for the technical support in confocal microscopy. We are also grateful for the computational support from HPC Platform and MHPC Laboratory of ShanghaiTech University. This work was supported by the National Key Research and Development Program of China (2023YFC2509800 to H.W., 2023YFC2508400 to Q.W.), the National Natural Science Foundation of China (82192861 and 82071051 to Z.X., 82222016 to H.W.), Shandong Provincial Natural Science Foundation (ZR2020ZD39 to Z.X.), the National Key R&D Program of China (no. 2022YFC3400501) and ShanghaiTech University's start package to F.B.

AUTHOR CONTRIBUTIONS

S.W. performed biochemical and structural experiments. L.L. solved, refined, and analyzed the crystal structures. Q.H. built the structure model and performed MD simulations. X.Y. and Y.X. conducted the immunostaining assays. S.L. and Q. Liu conducted the MET rescue experiments. H.W. and Q.W. collected and analyzed the patient data. S.W. and W.Z. performed NMR spectroscopy and analyzed the data. S.W., L.L., Q.H., H.W., Z.X., F.B., and Q. Lu analyzed the data and drafted the paper. All authors commented on the paper. Q. Lu coordinated the project.

DECLARATION OF INTERESTS

The authors declare no competing interests.

STAR★METHODS

Detailed methods are provided in the online version of this paper and include the following:

- KEY RESOURCES TABLE
- EXPERIMENTAL MODEL AND STUDY PARTICIPANT DETAILS
  - Mice
- METHOD DETAILS
  - Plasmids Construction, protein expression, and purification
  - Crystallization, data collection, and structure determination
  - Isothermal titration calorimetry assay
  - Inductively coupled plasma-Mass Spectrometry (ICP-MS)
  - SEC coupled with multi-angle static light scattering
  - NMR spectroscopy
  - Co-immunoprecipitation and western blotting
  - Injectorporation and whole-mount immunostaining
  - Whole-cell electrophysiology of hair cells
  - Complexes modeling and MD simulations
- QUANTIFICATION AND STATISTICAL ANALYSIS

SUPPLEMENTAL INFORMATION

Supplemental information can be found online at https://doi.org/10.1016/j.devcel.2025.01.004.

Received: June 22, 2023
Revised: August 20, 2024
Accepted: January 9, 2025
Published: January 30, 2025

REFERENCES

1. Azaiez, H., Booth, K.T., Ephraim, S.S., Crone, B., Black-Ziegelbein, E.A., Marini, R.J., Shearer, A.E., Sloan-Heggen, C.M., Kolbe, D., Casavant, T., et al. (2018). Genomic landscape and mutational signatures of deafness-associated genes. Am. J. Hum. Genet. *103*, 484–497. https://doi.org/10.1016/j.ajhg.2018.08.006.
2. Kitajiri, S.I., McNamara, R., Makishima, T., Husnain, T., Zafar, A.U., Kittles, R.A., Ahmed, Z.M., Friedman, T.B., Riazuddin, S., and Griffith, A.J. (2007). Identities, frequencies and origins of TMC1 mutations causing DFNB7/B11 deafness in Pakistan. Clin. Genet. *72*, 546–550. https://doi.org/10.1111/j.1399-0004.2007.00895.x.
3. Kalay, E., Karaguzel, A., Caylan, R., Heister, A., Cremers, F.P.M., Cremers, C.W.R.J., Brunner, H.G., de Brouwer, A.P.M., and Kremer, H. (2005). Four novel TMC1 (DFNB7/DFNB11) mutations in Turkish patients with congenital autosomal recessive nonsyndromic hearing loss. Hum. Mutat. *26*, 591. https://doi.org/10.1002/humu.9384.
4. Sirmaci, A., Duman, D., Oztürkmen-Akay, H., Erbek, S., Incesulu, A., Oztürk-Hişmi, B., Arici, Z.S., Yüksel-Konuk, E.B., Taşir-Yilmaz, S., Tokgöz-Yilmaz, S., et al. (2009). Mutations in TMC1 contribute significantly to nonsyndromic autosomal recessive sensorineural hearing loss: A report of five novel mutations. Int. J. Pediatr. Otorhinolaryngol. *73*, 699–705. https://doi.org/10.1016/j.ijporl.2009.01.005.
5. Tlili, A., Rebeh, I.B., Aifa-Hmani, M., Dhouib, H., Moalla, J., Tlili-Chouchène, J., Said, M.B., Lahmar, I., Benzina, Z., Charfedine, I., et al. (2008). TMC1 but not TMC2 is responsible for autosomal recessive nonsyndromic hearing impairment in Tunisian families. Audiol. Neurootol. *13*, 213–218. https://doi.org/10.1159/000115430.
6. Schrauwen, I., Sommen, M., Corneveaux, J.J., Reiman, R.A., Hackett, N.J., Claes, C., Claes, K., Bitner-Glindzicz, M., Coucke, P., Van Camp, G., et al. (2013). A sensitive and specific diagnostic test for hearing loss using a microdroplet PCR-based approach and next generation sequencing. Am. J. Med. Genet. A *161A*, 145–152. https://doi.org/10.1002/ajmg.a.35737.
7. Hilgert, N., Smith, R.J.H., and Van Camp, G. (2009). Forty-six genes causing nonsyndromic hearing impairment: which ones should be analyzed in DNA diagnostics? Mutat. Res. *681*, 189–196. https://doi.org/10.1016/j.mrrev.2008.08.002.
8. Vreugde, S., Erven, A., Kros, C.J., Marcotti, W., Fuchs, H., Kurima, K., Wilcox, E.R., Friedman, T.B., Griffith, A.J., Balling, R., et al. (2002). Beethoven, a mouse model for dominant, progressive hearing loss DFNA36. Nat. Genet. *30*, 257–258. https://doi.org/10.1038/ng848.
9. Wang, H.Y., Wu, K.W., Guan, J., Yang, J., Xie, L.Y., Xiong, F., Lan, L., Wang, D.Y., and Wang, Q.J. (2018). Identification of four TMC1 variations in different Chinese families with hereditary hearing loss. Mol. Genet. Genomic Med. *6*, 504–513. https://doi.org/10.1002/mgg3.394.
10. Hilgert, N., Alasti, F., Dieltjens, N., Pawlik, B., Wollnik, B., Uyguner, O., Delmaghani, S., Weil, D., Petit, C., Danis, E., et al. (2008). Mutation analysis of TMC1 identifies four new mutations and suggests an additional deafness gene at loci DFNA36 and DFNB7/11. Clin. Genet. *74*, 223–232. https://doi.org/10.1111/j.1399-0004.2008.01053.x.
11. Kurima, K., Peters, L.M., Yang, Y., Riazuddin, S., Ahmed, Z.M., Naz, S., Arnaud, D., Drury, S., Mo, J., Makishima, T., et al. (2002). Dominant and recessive deafness caused by mutations of a novel gene, TMC1, required for cochlear hair-cell function. Nat. Genet. *30*, 277–284. https://doi.org/10.1038/ng842.
12. Hildebrand, M.S., Kahrizi, K., Bromhead, C.J., Shearer, A.E., Webster, J.A., Khodaei, H., Abtahi, R., Bazazzadegan, N., Babanejad, M., Nikzat, N., et al. (2010). Mutations in TMC1 are a common cause of DFNB7/11 hearing loss in the Iranian population. Ann. Otol. Rhinol. Laryngol. *119*, 830–835. https://doi.org/10.1177/000348941011901207.
13. Nakanishi, H., Kurima, K., Kawashima, Y., and Griffith, A.J. (2014). Mutations of TMC1 cause deafness by disrupting mechanoelectrical transduction. Auris Nasus Larynx *41*, 399–408. https://doi.org/10.1016/j.anl.2014.04.001.
14. Corey, D.P., and Hudspeth, A.J. (1979). Response latency of vertebrate hair cells. Biophys. J. *26*, 499–506. https://doi.org/10.1016/S0006-3495(79)85267-4.
15. Hudspeth, A.J., and Jacobs, R. (1979). Stereocilia mediate transduction in vertebrate hair cells (auditory system/cilium/vestibular system). Proc. Natl. Acad. Sci. USA *76*, 1506–1509. https://doi.org/10.1073/pnas.76.3.1506.
16. Zheng, W., and Holt, J.R. (2021). The mechanosensory transduction machinery in inner ear hair cells. Annu. Rev. Biophys. *50*, 31–51. https://doi.org/10.1146/annurev-biophys-062420-081842.
17. Fettiplace, R., and Kim, K.X. (2014). The physiology of mechanoelectrical transduction channels in hearing. Physiol. Rev. *94*, 951–986. https://doi.org/10.1152/physrev.00038.2013.
18. Kurima, K., Ebrahim, S., Pan, B.F., Sedlacek, M., SenGupta, P., Millis, B.A., Cui, R.J., Nakanishi, H., Fujikawa, T., Kawashima, Y., et al. (2015). TMC1 and TMC2 localize at the site of mechanotransduction in mammalian inner ear hair cell stereocilia. Cell Rep. *12*, 1606–1617. https://doi.org/10.1016/j.celrep.2015.07.058.
19. Pan, B., Akyuz, N., Liu, X.P., Asai, Y., Nist-Lund, C., Kurima, K., Derfler, B.H., György, B., Limapichat, W., Walujkar, S., et al. (2018). TMC1 forms the pore of mechanosensory transduction channels in vertebrate inner ear hair cells. Neuron *99*, 736–753.e6. https://doi.org/10.1016/j.neuron.2018.07.033.
20. Pan, B., Géléoc, G.S., Asai, Y., Horwitz, G.C., Kurima, K., Ishikawa, K., Kawashima, Y., Griffith, A.J., and Holt, J.R. (2013). TMC1 and TMC2 are components of the mechanotransduction channel in hair cells of the mammalian inner ear. Neuron *79*, 504–515. https://doi.org/10.1016/j.neuron.2013.06.019.
21. Siemens, J., Lillo, C., Dumont, R.A., Reynolds, A., Williams, D.S., Gillespie, P.G., and Müller, U. (2004). Cadherin 23 is a component of the tip link in hair-cell stereocilia. Nature *428*, 950–955. https://doi.org/10.1038/nature02483.
22. Ahmed, Z.M., Goodyear, R., Riazuddin, S., Lagziel, A., Legan, P.K., Behra, M., Burgess, S.M., Lilley, K.S., Wilcox, E.R., Riazuddin, S., et al. (2006). The tip-link antigen, a protein associated with the transduction complex of sensory hair cells, is protocadherin-15. J. Neurosci. *26*, 7022–7034. https://doi.org/10.1523/JNEUROSCI.1163-06.2006.
23. Kazmierczak, P., Sakaguchi, H., Tokita, J., Wilson-Kubalek, E.M., Milligan, R.A., Müller, U., and Kachar, B. (2007). Cadherin 23 and protocadherin 15 interact to form tip-link filaments in sensory hair cells. Nature *449*, 87–91. https://doi.org/10.1038/nature06091.
24. Xiong, W., Grillet, N., Elledge, H.M., Wagner, T.F.J., Zhao, B., Johnson, K.R., Kazmierczak, P., and Müller, U. (2012). TMHS is an integral component of the mechanotransduction machinery of cochlear hair cells. Cell *151*, 1283–1295. https://doi.org/10.1016/j.cell.2012.10.041.
25. Qiu, X., Liang, X., Llongueras, J.P., Cunningham, C., and Müller, U. (2023). The tetraspan LHFPL5 is critical to establish maximal force sensitivity of the mechanotransduction channel of cochlear hair cells. Cell Rep. *42*, 112245. https://doi.org/10.1016/j.celrep.2023.112245.
26. Zhao, B., Wu, Z.Z., Grillet, N., Yan, L.X., Xiong, W., Harkins-Perry, S., and Müller, U. (2014). TMIE is an essential component of the mechanotransduction machinery of cochlear hair cells. Neuron *84*, 954–967. https://doi.org/10.1016/j.neuron.2014.10.041.
27. Cunningham, C.L., Qiu, X., Wu, Z., Zhao, B., Peng, G., Kim, Y.-H., Lauer, A., and Müller, U. (2020). TMIE defines pore and gating properties of the mechanotransduction channel of mammalian cochlear hair cells. Neuron *107*, 126–143.e8. https://doi.org/10.1016/j.neuron.2020.03.033.
28. Blazejczyk, M., Sobczak, A., Debowska, K., Wisniewska, M.B., Kirilenko, A., Pikula, S., Jaworski, J., Kuznicki, J., and Wojda, U. (2009). Biochemical characterization and expression analysis of a novel EF-hand Ca2+ binding protein calmyrin2 (Cib2) in brain indicates its function in NMDA receptor mediated Ca2+ signaling. Arch. Biochem. Biophys. *487*, 66–78. https://doi.org/10.1016/j.abb.2009.05.002.
29. Giese, A.P.J., Tang, Y.Q., Sinha, G.P., Bowl, M.R., Goldring, A.C., Parker, A., Freeman, M.J., Brown, S.D.M., Riazuddin, S., Fettiplace, R., et al. (2017). CIB2 interacts with TMC1 and TMC2 and is essential for

mechanotransduction in auditory hair cells. Nat. Commun. *8*, 43. https://doi.org/10.1038/s41467-017-00061-1.

30. Liang, X., Qiu, X., Dionne, G., Cunningham, C.L., Pucak, M.L., Peng, G., Kim, Y.H., Lauer, A., Shapiro, L., and Müller, U. (2021). CIB2 and CIB3 are auxiliary subunits of the mechanotransduction channel of hair cells. Neuron *109*, 2131–2149.e15. https://doi.org/10.1016/j.neuron.2021.05.007.
31. Wang, X., Liu, S., Cheng, Q., Qu, C., Ren, R., Du, H., Li, N., Yan, K., Wang, Y., Xiong, W., et al. (2023). CIB2 and CIB3 regulate stereocilia maintenance and mechanoelectrical transduction in mouse vestibular hair cells. J. Neurosci. *43*, 3219–3231. https://doi.org/10.1523/JNEUROSCI.1807-22.2023.
32. Jia, Y.Y., Zhao, Y.M., Kusakizako, T., Wang, Y., Pan, C.F., Zhang, Y.W., Nureki, O., Hattori, M., and Yan, Z.Q. (2020). TMC1 and TMC2 proteins are pore-forming subunits of mechanosensitive ion channels. Neuron *105*, 310–321.e3. https://doi.org/10.1016/j.neuron.2019.10.017.
33. Ballesteros, A., Fenollar-Ferrer, C., and Swartz, K.J. (2018). Structural relationship between the putative hair cell mechanotransduction channel TMC1 and TMEM16 proteins. eLife *7*, e38433. https://doi.org/10.7554/eLife.38433.
34. Akyuz, N., Karavitaki, K.D., Pan, B.F., Tamvakologos, P.I., Brock, K.P., Li, Y.Q., Marks, D.S., and Corey, D.P. (2022). Mechanical gating of the auditory transduction channel TMC1 involves the fourth and sixth transmembrane helices. Sci. Adv. *8*, eabo1126. https://doi.org/10.1126/sciadv.abo1126.
35. Fu, S., Pan, X., Lu, M., Dong, J., and Yan, Z. (2024). Human TMC1 and TMC2 are mechanically gated ion channels. Neuron. https://doi.org/10.1016/j.neuron.2024.11.009.
36. Tang, Y.Q., Lee, S.A., Rahman, M., Vanapalli, S.A., Lu, H., and Schafer, W.R. (2020). Ankyrin is an intracellular tether for TMC mechanotransduction channels. Neuron *107*, 112–125.e10. https://doi.org/10.1016/j.neuron.2020.03.026.
37. Giese, A.P.J., Weng, W.H., Kindt, K.S., Chang, H.H.V., Montgomery, J.S., Ratzan, E.M., Beirl, A.J., Aponte Rivera, R., Lotthammer, J.M., Walujkar, S., et al. (2025). Complexes of vertebrate TMC1/2 and CIB2/3 proteins form hair-cell mechanotransduction cation channels. Elife *12*, RP89719. https://doi.org/10.7554/eLife.89719.
38. Wang, Y.F., Li, J., Yao, X.R., Li, W., Du, H.B., Tang, M.L., Xiong, W., Chai, R.J., and Xu, Z.G. (2017). Loss of CIB2 causes profound hearing loss and abolishes mechanoelectrical transduction in mice. Front. Mol. Neurosci. *10*, 401. https://doi.org/10.3389/fnmol.2017.00401.
39. Michel, V., Booth, K.T., Patni, P., Cortese, M., Azaiez, H., Bahloul, A., Kahrizi, K., Labbé, M., Emptoz, A., Lelli, A., et al. (2017). CIB2, defective in isolated deafness, is key for auditory hair cell mechanotransduction and survival. EMBO Mol. Med. *9*, 1711–1731. https://doi.org/10.15252/emmm.201708087.
40. Marcotti, W., Erven, A., Johnson, S.L., Steel, K.P., and Kros, C.J. (2006). Tmc1 is necessary for normal functional maturation and survival of inner and outer hair cells in the mouse cochlea. J. Physiol. *574*, 677–698. https://doi.org/10.1113/jphysiol.2005.095661.
41. Beurg, M., Barlow, A., Furness, D.N., and Fettiplace, R. (2019). A Tmc1 mutation reduces calcium permeability and expression of mechanoelectrical transduction channels in cochlear hair cells. Proc. Natl. Acad. Sci. USA *116*, 20743–20749. https://doi.org/10.1073/pnas.1908058116.
42. Jeong, H., Clark, S., Goehring, A., Dehghani-Ghahnaviyeh, S., Rasouli, A., Tajkhorshid, E., and Gouaux, E. (2022). Structures of the TMC-1 complex illuminate mechanosensory transduction. Nature *610*, 796–803. https://doi.org/10.1038/s41586-022-05314-8.
43. Clark, S., Jeong, H., Posert, R., Goehring, A., and Gouaux, E. (2024). The structure of the Caenorhabditis elegans TMC-2 complex suggests roles of lipid-mediated subunit contacts in mechanosensory transduction. Proc. Natl. Acad. Sci. USA *121*, e2314096121. https://doi.org/10.1073/pnas.2314096121.
44. Marquis, R.E., and Hudspeth, A.J. (1997). Effects of extracellular Ca2+ concentration on hair-bundle stiffness and gating-spring integrity in hair cells. Proc. Natl. Acad. Sci. USA *94*, 11923–11928. https://doi.org/10.1073/pnas.94.22.11923.
45. Hacohen, N., Assad, J.A., Smith, W.J., and Corey, D.P. (1989). Regulation of tension on hair-cell transduction channels: displacement and calcium dependence. J. Neurosci. *9*, 3988–3997. https://doi.org/10.1523/JNEUROSCI.09-11-03988.1989.
46. Kennedy, H.J., Evans, M.G., Crawford, A.C., and Fettiplace, R. (2003). Fast adaptation of mechanoelectrical transducer channels in mammalian cochlear hair cells. Nat. Neurosci. *6*, 832–836. https://doi.org/10.1038/nn1089.
47. Beurg, M., Nam, J.H., Crawford, A., and Fettiplace, R. (2008). The actions of calcium on hair bundle mechanics in mammalian cochlear hair cells. Biophys. J. *94*, 2639–2653. https://doi.org/10.1529/biophysj.107.123257.
48. Corns, L.F., Johnson, S.L., Kros, C.J., and Marcotti, W. (2014). Calcium entry into stereocilia drives adaptation of the mechanoelectrical transducer current of mammalian cochlear hair cells. Proc. Natl. Acad. Sci. USA *111*, 14918–14923. https://doi.org/10.1073/pnas.1409920111.
49. Peng, A.W., Effertz, T., and Ricci, A.J. (2013). Adaptation of mammalian auditory hair cell mechanotransduction is independent of calcium entry. Neuron *80*, 960–972. https://doi.org/10.1016/j.neuron.2013.08.025.
50. Caprara, G.A., Mecca, A.A., Wang, Y., Ricci, A.J., and Peng, A.W. (2019). Hair bundle stimulation mode modifies manifestations of mechanotransduction adaptation. J. Neurosci. *39*, 9098–9106. https://doi.org/10.1523/JNEUROSCI.1408-19.2019.
51. Bosher, S.K., and Warren, R.L. (1978). Very low calcium content of cochlear endolymph, an extracellular fluid. Nature *273*, 377–378. https://doi.org/10.1038/273377a0.
52. Huang, H., Bogstie, J.N., and Vogel, H.J. (2012). Biophysical and structural studies of the human calcium- and integrin-binding protein family: understanding their functional similarities and differences. Biochem. Cell Biol. *90*, 646–656. https://doi.org/10.1139/o2012-021.
53. Ames, J.B. (2021). L-type Ca2+ channel regulation by calmodulin and CaBP1. Biomolecules *11*, 1811. https://doi.org/10.3390/biom11121811.
54. Banerjee, R., Yoder, J.B., Yue, D.T., Amzel, L.M., Tomaselli, G.F., Gabelli, S.B., and Ben-Johny, M. (2018). Bilobal architecture is a requirement for calmodulin signaling to Ca(V)1.3 channels. Proc. Natl. Acad. Sci. USA *115*, E3026–E3035. https://doi.org/10.1073/pnas.1716381115.
55. Ben-Johny, M., Yang, P.S., Niu, J., Yang, W.J., Joshi-Mukherjee, R., and Yue, D.T. (2014). Conservation of Ca2+/calmodulin regulation across Na and Ca2+ channels. Cell *157*, 1657–1670. https://doi.org/10.1016/j.cell.2014.04.035.
56. Peterson, B.Z., DeMaria, C.D., Adelman, J.P., and Yue, D.T. (1999). Calmodulin is the Ca2+ sensor for Ca2+-dependent inactivation of 1-type calcium channels. Neuron *22*, 549–558. https://doi.org/10.1016/s0896-6273(00)80709-6.
57. Villarroel, A., Taglialatela, M., Bernardo-Seisdedos, G., Alaimo, A., Agirre, J., Alberdi, A., Gomis-Perez, C., Soldovieri, M.V., Ambrosino, P., Malo, C., et al. (2014). The ever changing moods of calmodulin: how structural plasticity entails transductional adaptability. J. Mol. Biol. *426*, 2717–2735. https://doi.org/10.1016/j.jmb.2014.05.016.
58. Villalobo, A., Ishida, H., Vogel, H.J., and Berchtold, M.W. (2018). Calmodulin as a protein linker and a regulator of adaptor/scaffold proteins. Biochim. Biophys. Acta Mol. Cell Res. *1865*, 507–521. https://doi.org/10.1016/j.bbamcr.2017.12.004.
59. Marshall, C.B., Nishikawa, T., Osawa, M., Stathopulos, P.B., and Ikura, M. (2015). Calmodulin and STIM proteins: two major calcium sensors in the cytoplasm and endoplasmic reticulum. Biochem. Biophys. Res. Commun. *460*, 5–21. https://doi.org/10.1016/j.bbrc.2015.01.106.
60. Fettiplace, R., Furness, D.N., and Beurg, M. (2022). The conductance and organization of the TMC1-containing mechanotransducer channel complex in auditory hair cells. Proc. Natl. Acad. Sci. USA *119*, e2210849119. https://doi.org/10.1073/pnas.2210849119.
61. Beurg, M., Cui, R., Goldring, A.C., Ebrahim, S., Fettiplace, R., and Kachar, B. (2018). Variable number of TMC1-dependent mechanotransducer

channels underlie tonotopic conductance gradients in the cochlea. Nat. Commun. *9*, 2185. https://doi.org/10.1038/s41467-018-04589-8.

62. Berridge, M.J., Bootman, M.D., and Lipp, P. (1998). Calcium - a life and death signal. Nature *395*, 645–648. https://doi.org/10.1038/27094.
63. Vallone, R., Dal Cortivo, G., D'Onofrio, M., and Dell'Orco, D. (2018). Preferential binding of Mg(2+) over Ca(2+) to CIB2 triggers an allosteric switch impaired in Usher syndrome type 1J. Front. Mol. Neurosci. *11*, 274. https://doi.org/10.3389/fnmol.2018.00274.
64. Evans, R., O'Neill, M., Pritzel, A., Antropova, N., Senior, A., Green, T., Žídek, A., Bates, R., Blackwell, S., Yim, J., et al. (2022). Protein complex prediction with AlphaFold-Multimer. Preprint at bioRxiv,. https://doi.org/10.1101/2021.10.04.463034.
65. Jo, S., Kim, T., Iyer, V.G., and Im, W. (2008). CHARMM-GUI: a web-based graphical user interface for CHARMM. J. Comput. Chem. *29*, 1859–1865. https://doi.org/10.1002/jcc.20945.
66. Hess, B., Kutzner, C., van der Spoel, D., and Lindahl, E. (2008). GROMACS 4: Algorithms for highly efficient, load-balanced, and scalable molecular simulation. J. Chem. Theor. Comput. *4*, 435–447. https://doi.org/10.1021/ct700301q.
67. Klauda, J.B., Venable, R.M., Freites, J.A., O'Connor, J.W., Tobias, D.J., Mondragon-Ramirez, C., Vorobyov, I., MacKerell, A.D., and Pastor, R.W. (2010). Update of the CHARMM all-atom additive force field for lipids: validation on six lipid types. J. Phys. Chem. B *114*, 7830–7843. https://doi.org/10.1021/jp101759q.
68. Jorgensen, W.L., Chandrasekhar, J., Madura, J.D., Impey, R.W., and Klein, M.L. (1983). Comparison of simple potential functions for simulating liquid water. J. Chem. Phys. (USA) *79*, 926–935. https://doi.org/10.1063/1.445869.
69. Hu, Q.Y., Padron, K., Hara, D., Shi, J.W., Pollack, A., Prabhakar, R., and Tao, W.S. (2021). Interactions of urea-based inhibitors with prostate-specific membrane antigen for boron neutron capture therapy. ACS Omega *6*, 33354–33369. https://doi.org/10.1021/acsomega.1c03554.
70. Paul, T.J., Parac-Vogt, T.N., Quiñonero, D., and Prabhakar, R. (2018). Investigating polyoxometalate-protein interactions at chemically distinct binding sites. J. Phys. Chem. B *122*, 7219–7232. https://doi.org/10.1021/acs.jpcb.8b02931.
71. Katsuta, H., Sawada, Y., and Sokabe, M. (2019). Biophysical mechanisms of membrane-thickness-dependent MscL gating: an all-atom Molecular Dynamics study. Langmuir *35*, 7432–7442. https://doi.org/10.1021/acs.langmuir.8b02074.
72. Gentry, H.R., Singer, A.U., Betts, L., Yang, C., Ferrara, J.D., Sondek, J., and Parise, L.V. (2005). Structural and biochemical characterization of CIB1 delineates a new family of EF-hand-containing proteins. J. Biol. Chem. *280*, 8407–8415. https://doi.org/10.1074/jbc.M411515200.
73. Yu, X., Zhao, Q., Li, X., Chen, Y., Tian, Y., Liu, S., Xiong, W., and Huang, P. (2020). Deafness mutation D572N of TMC1 destabilizes TMC1 expression by disrupting LHFPL5 binding. Proc. Natl. Acad. Sci. USA *117*, 29894–29903. https://doi.org/10.1073/pnas.2011147117.
74. Aristizábal-Ramírez, I., Dragich, A.K., Giese, A.P.J., Sofia Zuluaga-Osorio, K., Watkins, J., Davies, G.K., Hadi, S.E., Riazuddin, S., Vander Kooi, C.W., Ahmed, Z.M., et al. (2023). Calcium and integrin-binding protein 2 (CIB2) controls force sensitivity of the mechanotransducer channels in cochlear outer hair cells. Preprint at bioRxiv. https://doi.org/10.1101/2023.07.09.545606.
75. Jung, J., and Müller, U. (2023). Mechanoelectrical transduction-related genetic forms of hearing loss. Curr. Opin. Physiol. *32*, 100632. https://doi.org/10.1016/j.cophys.2023.100632.
76. Nishio, S.-Y., and Usami, S.-I. (2022). Prevalence and clinical features of autosomal dominant and recessive TMC1-associated hearing loss. Hum. Genet. *141*, 929–937. https://doi.org/10.1007/s00439-021-02364-2.
77. Agirre, J., Atanasova, M., Bagdonas, H., Ballard, C.B., Baslé, A., Beilsten-Edmands, J., Borges, R.J., Brown, D.G., Burgos-Mármol, J.J., Berrisford, J.M., et al. (2023). The CCP4 suite: integrative software for macromolecular crystallography. Acta Crystallogr. D Struct. Biol. *79*, 449–461. https://doi.org/10.1107/S2059798323003595.
78. McCoy, A.J., Grosse-Kunstleve, R.W., Adams, P.D., Winn, M.D., Storoni, L.C., and Read, R.J. (2007). Phaser crystallographic software. J. Appl. Crystallogr. *40*, 658–674. https://doi.org/10.1107/S0021889807021206.
79. Liebschner, D., Afonine, P.V., Baker, M.L., Bunkóczi, G., Chen, V.B., Croll, T.I., Hintze, B., Hung, L.W., Jain, S., McCoy, A.J., et al. (2019). Macromolecular structure determination using X-rays, neutrons and electrons: recent developments in Phenix. Acta Crystallogr. D Struct. Biol. *75*, 861–877. https://doi.org/10.1107/S2059798319011471.
80. Emsley, P., and Cowtan, K. (2004). Coot: model-building tools for molecular graphics. Acta Crystallogr. D Biol. Crystallogr. *60*, 2126–2132. https://doi.org/10.1107/S0907444904019158.
81. Minor, W., Cymborowski, M., Otwinowski, Z., and Chruszcz, M. (2006). HKL-3000: the integration of data reduction and structure solution - from diffraction images to an initial model in minutes. Acta Crystallogr. D Biol. Crystallogr. *62*, 859–866. https://doi.org/10.1107/S0907444906019949.
82. Du, H., Zou, L., Ren, R., Li, N., Li, J., Wang, Y., Sun, J., Yang, J., Xiong, W., and Xu, Z. (2020). Lack of PDZD7 long isoform disrupts ankle-link complex and causes hearing loss in mice. FASEB J. *34*, 1136–1149. https://doi.org/10.1096/fj.201901657RR.
83. Sehnal, D., Svobodová Vařeková, R., Berka, K., Pravda, L., Navrátilová, V., Banáš, P., Ionescu, C.M., Otyepka, M., and Koča, J. (2013). MOLE 2.0: advanced approach for analysis of biomacromolecular channels. J. Cheminform. *5*, 39. https://doi.org/10.1186/1758-2946-5-39.

STAR★METHODS

KEY RESOURCES TABLE

REAGENT or RESOURCE	SOURCE	IDENTIFIER
Antibodies		
Rabbit anti-DYKDDDDK Tag (D6W5B) antibody	Cell Signaling Technology	Cat# 14793; RRID: AB_2572291
Anti-GFP	Santa Cruz biotechnology	Cat# Sc-9996; RRID: AB_627695
Anti-GFP	Abcam	Cat# ab290; RRID: AB_303395
Goat anti-Mouse IgG (H+L) Secondary Antibody, HRP	invitrogen	Cat# 31430; RRID: AB_228307
Goat anti-Rabbit IgG (H+L) Secondary Antibody, HRP	invitrogen	Cat# 31460; RRID: AB_228341
Anti-GAPDH	Proteintech	Cat# 60004-1-Ig; RRID: AB_2107436
Biological samples		
The cochlea of C57BL/6J mice	Chinese Institute for Brain research, Beijing, Laboratory Animal Resource Center	JAX Stock No: 000664
Chemicals, peptides, and recombinant proteins		
Recombinant proteins: TMC1 full-length, CR1, CR2, CR3(Uniprot: Q8R4P5;1-757,81-130,298-352;718-757)	This paper	N/A
Recombinant proteins: TMC1 full-length mutants, ΔCR1, ΔCR2, ΔCR3(Uniprot: Q8R4P5; Δ81-130, Δ298-352; Δ718-757)	This paper	N/A
Recombinant proteins: TMC1 full-length mutants, ΔCR1/2, ΔCR1/3, ΔCR1/2/3(Uniprot: Q8R4P5; Δ81-130+298-352; Δ81-130+718-757; Δ81-130+298-352+718-757)	This paper	N/A
Recombinant protein: CIB2 full-length (Uniprot: Q9Z309, 1-187)	This paper	N/A
TRITC-conjugated phalloidin	Sigma-Aldrich	Cat# P1951
HBSS	gibco	Cat# 14175095
DMEM/F12	gibco	Cat# 21041025
CaCl2·2H2O	Sigma	Cat# C7902-500G
BSA	Sigma	Cat# A9418-100G
Tween-20	Sigma	Cat# P1379-25ML
EDTA	Sinopharm Chemical Reagent	Cat# 10009617
Triton X-100	Sigma-Aldrich	Cat# T8787
Lipofectamine 3000	Invitrogen	Cat# L3000015
Critical commercial assays		
EndoFree Mini Plasmid Kit	TIANGEN	Cat# DP123-02
FastPure Gel DNA Extraction Mini Kit	Vazyme	Cat# DC301
Deposited data		
CIB2-TMC1 CR1 structure	This paper	PDB: 8Z3F
Experimental models: Cell lines		
Human: HEK293T cells	ATCC	CRL-3216; RRID: CVCL_0063
Experimental models: Organisms/strains		
Escherichia coli BL21 (DE3) cells	Invitrogen	Cat# C600003
Mouse: C57BL/6J	Cyagen	N/A

(*Continued on next page*)

Continued

REAGENT or RESOURCE	SOURCE	IDENTIFIER
Oligonucleotides		
See Table S4	Biosune, China	N/A
Recombinant DNA		
Plasmid for recombinant protein expression: 32m3c-CIB2 full-length, CIB2-DD116/120AA, DD157/161AA, E64D, R66W, F91S, I123T, E141N	This paper	N/A
Plasmid for recombinant protein expression: 32m3c- TMC1-CR1, TMC1-CR2, TMC1-CR3	This paper	N/A
Plasmid for recombinant protein expression: 32m3c- TMC1-CR1-M107I	This paper	N/A
Plasmid for recombinant protein expression: 32m3c-TMC1-CR2-F307S; 32m3c-TMC1-CR2-S314R	This paper	N/A
Plasmid for recombinant protein expression: pMal-c2X- TMC1 CR2	This paper	N/A
Plasmid for heterologous cells transfection: pFLAG-CMV2-CIB2	This paper	N/A
Plasmid for heterologous cells transfection: eGFP-TMC1 full length, ΔCR1, ΔCR2, ΔCR3, ΔCR1/2, ΔCR1/3, ΔCR1/2/3	This paper	N/A
Plasmid for Mice cochlear transfection: pcDNA3.1-CIB2 wild type, CIB2-DD116/120AA, CIB2-DD157/161AA	This paper	N/A
Software and algorithms		
ImageJ	NIH	https://imagej.net/
PyMOL	Molecular Graphics System, Schrodinger, LLC	https://pymol.org/2/
CCP4	Agirre et al.[77]	http://www.ccp4.ac.uk
PHASER	McCoy et al.[78]	http://www.phaser.cimr.cam.ac.uk/index.php/Phaser_Crystallographic_Software
PHENIX	Liebschner et al.[79]	https://www.phenix-online.org/
COOT	Emsley and Cowtan[80]	http://www2.mrc-lmb.cam.ac.uk/personal/pemsley/coot/
Prism	GraphPad	https://www.graphpad.com/ scientific-software/prism/
GROMACS	University of Groningen	https://www.gromacs.org/
CHARMM-GUI	Lehigh University	https://www.charmm-gui.org/

EXPERIMENTAL MODEL AND STUDY PARTICIPANT DETAILS

Mice

All experiments were conducted in compliance with the ARRIVE guidelines 2.0 and approved by the Animal Ethics Committee of Shandong University School of Life Sciences (Permit Number: SYDWLL-2021-74). Mice were housed in a controlled environment with a 12-h light/dark cycle. Food and water were available *ad libitum* in individual cages with bedding materials. Mice of either sex were used in the present study and were handled with caution to minimize stress. *Cib2*$^{-/-}$ mice were maintained and genotyped as previously reported.[38]

METHOD DETAILS

Plasmids Construction, protein expression, and purification

We produced different constructs of CIB2 (reference number UniProt: Q9Z309) and TMC1 (reference number UniProt: Q8R4P5) using standard PCR (Vazyme, Nanjing, China) and homologous recombination (Yeasen, Shanghai, China). All point mutations and disease mutations of CIB2 and TMC1 described in this study were introduced using the PCR-based mutagenesis method. Both

primers and DNA sequencing were provided by GENEWIZ (Suzhou, China) and BioSune (Shanghai, China). CIB2, TMC1 CR1 (amino acids 81-130), TMC1 CR2 (amino acids 298-352), TMC1 CR3 (amino acids 718-757), and all point mutations and disease mutations of CIB2 and TMC1 were cloned into the appropriate expression vectors, pET.32m.3c with trx-6xhis tag, pMal-c2X with the mbp-6xhis tag, pEGFP-C1 with eGFP tag or pFLAG-CMV2 with flag tag, as required.

Recombinant proteins were expressed in *Escherichia coli* BL21 (DE3) cells grown in LB medium at 37°C until the OD_{600} values reached ~0.5. The BL21 cells were then induced with 1mM IPTG and incubated at 16°C for ~16-20 hours. Recombinant proteins were purified using Ni^{2+}-NTA agarose affinity column followed by size-exclusion chromatography (SEC) (Superdex 200 26/600 column from GE Healthcare). The purification buffer contained 50 mM Tris pH 7.8, 100 mM NaCl, 1 mM dithiothreitol (DTT), and 10 mM ethylenediaminetetraacetic acid (EDTA). In calcium state the buffer changes to 50 mM Tris, pH 7.5-8.0, 100 mM NaCl, and 10 mM $CaCl_2$. During crystallization, SEC-MALS, and NMR-based titration experiments, the N-Terminal Trx-His6 tag was removed by 3C protease and another step of SEC chromatography.

Crystallization, data collection, and structure determination

We did a point mutation at CIB2 p.E141 (mutated to Asparagine) to obtain high quality diffraction data (Figures S1 and S7B; Table S1). CIB2-E141N and TMC1 CR1 were copurified and were concentrated to a final concentration of 10 mg/ml for crystallization. Initial crystallization screening was performed with 96 conditions kits from HAMPTON. The complex grew at 16°C by the vapor diffusion method in sitting drops, in buffer containing 20% v/v 2-Proranol, 0.1 M MES monohydrate pH 6.0, and 20% w/v PEG monomethyl ether 2000. Crystals were cryoprotected in a reservoir solution with 20% glycerol. Diffraction data were collected at BL19U1 at Shanghai Synchrotron Radiation Facility (SSRF, Shanghai, China) and were processed with HKL3000.[81]

The structure was solved by PHASER in CCP4.[77,78] The crystal structure of CIB3 (PDB: 6WU5) was used as the search model. CCP4 Autobuild was used to improve the structure completeness, and further loop building and refinement were performed iteratively using Coot[80] and REFMAC PHENIX.[79] The final refinement statistics of the structure are listed in Table S2, and structural diagrams were prepared using PyMOL (http://www.pymol.org).

Isothermal titration calorimetry assay

The ITC measurements were carried out on a MicroCal ITC200 system (Malvern Panalytical) at 25°C. Approximately 300-500 μM of TMC1 truncations were loaded into the syringe and titrated into the cell ~30-50 μM protein of CIB2 WT or mutations. 10 mM EDTA/$CaCl_2$ were added in buffer. The concentration of Ca^{2+} or Mg^{2+} used in Figure S2A was 2 mM; in Figure S2B was 5 mM. We constructed TMC1 CR2 with maltose binding protein (MBP) tag to get monomer protein. Each titration point was acquired by injecting a 1-μl aliquot of the protein sample from the syringe into the protein sample in the cell. Titration data was analyzed using MicroCal PEAQ-ITC Analysis Software and fitted by the one-site binding model.

Inductively coupled plasma-Mass Spectrometry (ICP-MS)

The ICP-MS measurements were carried out on a NexION2000 (Flexar20 HPLC) system at 25°C.

We prepared CIB2 and CIB2 & TMC1 CR1 complex samples with 50 mM Tris pH 7.8, 100 mM NaCl, 1 mM dithiothreitol (DTT), and 10 mM ethylenediaminetetraacetic acid (EDTA) as described above to eliminate metal ions influences. The Trx-tags were removed by another SEC step using the same buffer without EDTA to remove the excess EDTA. The samples were concentrated to 300 μM, adding 1:1, 1:3, 1:5 or 1:10 molar radio with $CaCl_2$ or $MgCl_2$. Then we used desalting columns (GE Disposable PD-10) to remove the excess Ca^{2+} or Mg^{2+}. The ICP-MS measurements were performed by the Instrumental Analysis Center of SJTU, and data analysis was by GraphPad Prism 7.0.

SEC coupled with multi-angle static light scattering

A superose 12 10/300 GL column (GE Healthcare), a multi-angle static light scattering detector (miniDAWN, Wyatt), and a differential refractive index detector (Optilab, Wyatt) were coupled with the AKTA FPLC system. The column was pre-equilibrated overnight, and purified proteins were prepared at a concentration of ~300 μL and 100 μM for loading. Data was analyzed using ASTRA 6 (Wyatt).

NMR spectroscopy

Nuclear Magnetic Resonance (NMR) samples of CIB2 of 300 μM in complex with TMC-CR1 (residues 81-130) of 300 μM were prepared in buffer containing 50 mM Tris pH 7.0, 100 mM NaCl, 10 mM EDTA (*apo* state) or 10 mM $CaCl_2$ (calcium state) in 10% v/v D_2O. All NMR spectra were collected at 300K on Agilent VnmrS DD2 700MHz spectrometer equipped with a 5mm XYZ PFG HCN room temperature probe. Chemical shifts were referenced to external DSS. Spectra were processed using the program NMRPipe and analyzed with the program NMRFAM-SPARKY.

Co-immunoprecipitation and western blotting

HEK 293 cells were maintained at 37°C in 5% CO2 using DMEM (HyClone) supplemented with 10% FBS (Gibco), and 1% penicillin–streptomycin (Invitrogen). Cells were transfected with 3μg of each plasmid using Lipo 3000 (Invitrogen). After 24 hours, cells were washed with 1x PBS, then centrifuged at 12000 rpm for 10 min. Cells were lysed using a modified RIPA buffer containing 50 mM Tris (pH 8.0), 150 mM NaCl, 5 mM EDTA (*apo* state) or 5 mM $CaCl_2$ (calcium state), 1% Triton, 0.1% SDS and a Roche Complete Protease Inhibitor Tablet. Then cell lysates were rotated for 30 min at 4°C followed by centrifuged at 12000 rpm for 10 min at 4°C.

Cell lysates were immunoprecipitated for 1 hour at 4°C using 20 μL Anti-GFP Affinity Beads (Smart-Lifesciences, Changzhou, China). After immunoprecipitation, cell lysates were centrifuged at 3000 rpm for 3 min at 4°C and washed three times with RIPA buffer. 2x Loading Buffer was added into lysates and boiled for 10 min. SDS-PAGE was performed using 4-20% Tris-Glycine gel (Beyotime, Shanghai, China) and then transferred to PVDF membranes (Millipore). Membranes were block for 2 hours with 5% non-fat dry milk in 1x PBST containing 25 mM Tris (pH 7.5), 150 NaCl and 0.1% Tween-20. Membranes were incubated with Primary antibodies at 4°C overnight and incubated with secondary antibodies at RT for 1 hour after washed three times with 1x PBST. Membranes were finally washed and imaged with Chemiluminescent HRP Substrate (Millipore).

Primary antibodies were as follows: mouse anti-GFP (1:5000, Santa Cruz), rabbit anti-FLAG (1:4000, Cell signaling), mouse anti-GAPDH (1:5000, Proteintech, Wuhan, China). Secondary antibodies were goat anti-mouse (1:5000, Invitrogen) and goat anti-rabbit (1:5000, Invitrogen).

Injectorporation and whole-mount immunostaining

Injectorporation and whole-mount immunostaining was performed as previously described.[82] Briefly, cochlear sensory epithelia were dissected out of P3 wild-type mice followed by culturing in DMEM/F12 with 1.5 μg/mL ampicillin. GFP-CIB2 expression plasmids (1 μg/μL in 1× Hanks' balanced salt solution) were delivered to the sensory epithelia using a glass pipette (2 μm tip diameter). A series of three pulses at 60 V lasting 15 ms at 1-s intervals were applied to cochlear tissues using an electroporator (ECM Gemini X2, BTX, CA). After culturing for 1 day *in vitro*, the samples were fixed with 4% paraformaldehyde (PFA) in PBS for 20 min, then permeabilized and blocked with PBST (1% Triton X-100, and 5% donkey serum in PBS) for 1 hour. To visualize the stereociliary F-actin core, samples were then incubated with TRITC-conjugated phalloidin (Sigma-Aldrich, Cat. No. P1951, 1:1000 dilution) in PBS for 20 min at room temperature. The samples were mounted in PBS/glycerol (1:1) and imaged with a confocal microscope (LSM 900; Zeiss).

Whole-cell electrophysiology of hair cells

Cochleae of P3 *Cib2*$^{-/-}$ mice were dissected in dissection solution, which contains 141.7 mM NaCl, 5.36 mM KCl, 0.1 mM $CaCl_2$, 1 mM $MgCl_2$, 0.5 mM $MgSO_4$, 3.4 mM L-glutamine, 10 mM glucose, and 10 mM H-HEPES (pH=7.4). After injectoporation as described above, the basilar membrane was transferred into a recording chamber with recording solution, which contains 144 mM NaCl, 0.7 mM NaH_2PO_4, 5.8 mM KCl, 1.3 mM $CaCl_2$, 0.9 mM $MgCl_2$, 5.6 mM glucose, and 10 mM H-HEPES (pH=7.4). These acutely isolated sample need be recorded within 1 hour. Recording was performed under an upright microscope (BX51WI, Olympus, Tokyo, Japan) with a 60 × water immersion objective and an sCMOS camera (ORCA Flash4.0, Hamamatsu, Hamamatsu City, Japan) controlled by MicroManager 1.6 software. Patch pipettes resistances need to be controlled within 4-6 M'Ω. Intracellular solution contained (in mM): 140 mM KCl, 1mM $MgCl_2$, 0.1 mM EGTA, 2 mM Mg-ATP, 0.3 mM Na-GTP, and 10 mM H-HEPES, pH=7.2). Hair cells were recorded with a patch-clamp amplifier (EPC 10 USB and Patchmaster software, HEKA Elektronik, Lambrecht/Pfalz, Germany). MET was recorded by a 10 Hz sinusoidal wave delivered by a 27-mm-diameter piezoelectric disc driven by a home-made piezo amplifier pipette with a tip diameter of 3–5 μm positioned 5–10 μm from the hair bundle. Data were analyzed through Igor Pro 9, with self-made macros.

Complexes modeling and MD simulations

The structure model of human TMC1 dimer was obtained by utilizing the AlphaFold-Multimer with default model parameters and full genetic database.[64] The preparation of molecular dynamics (MD) input files of TMC1-CIB2 dimer was conducted through bilayer builder of CHARMM-GUI.[65] The following all-atom MD simulations were performed using the GROMACS program[66] and CHARMM36 force field.[67] To simulate the open state of TMC1 channel, -20 bar pressure was applied on the bilayer plane (*xy*-plane) while keeping the pressure in the normal (*z*) direction at 1 bar. The cross-sectional areas of protein complex were computed by CHARMM-GUI and the possible ion permeation pore of the TMC1 channel was determined by MOLE 2.0.[83]

QUANTIFICATION AND STATISTICAL ANALYSIS

Data analysis was conducted using GraphPad Prism software, with statistical details provided in the Results, Figures, and Figure Legends. All data are presented as mean ± SEM. For two-group comparisons in Figure S2C, statistical significance was assessed using a two-tailed unpaired Student's t-test (*, $p < 0.05$; **, $p < 0.01$; ***, $p < 0.001$). For comparisons involving more than two conditions in Figure 4E, one-way ANOVA followed by Dunn's multiple comparison test was applied (*, $p < 0.05$; **, $p < 0.01$; ***, $p < 0.001$). Exact values of n are reported where appropriate. Depending on the experiment, n represents number of animals or number of experiments.